A defining member of the new cysteine-cradle family is an aECM protein signalling skin damage in *C. elegans*

Thomas Sonntag[1], Shizue Omi[1], Antonina Andreeva[2], Jeanne Eichelbrenner[1], Andrew D. Chisholm[3], Jordan D. Ward[4], Nathalie Pujol[1,*]

[1] Aix Marseille Univ, INSERM, CNRS, CIML, Turing Centre for Living Systems, Marseille, France
[2] European Molecular Biology Laboratory, European Bioinformatics Institute (EMBL-EBI), Wellcome Genome Campus, Hinxton, Cambridgeshire CB10 1SD, UK
[3] Department of Cell and Developmental Biology, School of Biological Sciences, University of California San Diego, La Jolla, CA 92093, USA
[4] Department of Molecular, Cell, and Developmental Biology, University of California Santa Cruz, Santa Cruz, CA 95064, USA
* corresponding author

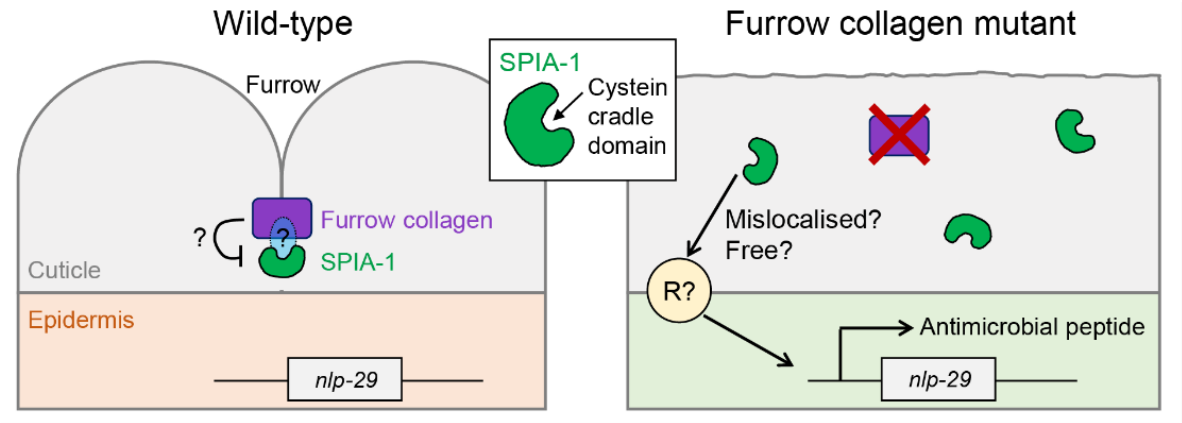

Abstract

Apical extracellular matrices (aECMs) act as crucial barriers, and communicate with the epidermis to trigger protective responses following injury or infection. In *Caenorhabditis elegans*, the skin aECM, the cuticle, is produced by the epidermis and is decorated with periodic circumferential furrows. We previously showed that mutants lacking cuticle furrows exhibit persistent immune activation (PIA). In a genetic suppressor screen, we identified *spia-1* as a key gene downstream of furrow collagens and upstream of immune signalling. *spia-1* expression oscillates during larval development, peaking between each moult together with patterning cuticular components. It encodes a secreted protein that localises to furrows. SPIA-1 shares a novel cysteine-cradle domain with other aECM proteins. SPIA-1 mediates immune activation in response to furrow loss and is proposed to act as a sensor of cuticle damage. This research provides a molecular insight into intricate interplay between cuticle integrity and epidermal immune activation in *C. elegans*.

Introduction

All multicellular organisms must protect themselves from injury and pathogens. *Caenorhabditis elegans* lacks an adaptive immune system and motile immune cells. Instead, it relies on its epithelial barriers to defend itself against environmental threats. This makes it a powerful model to address the question of how epithelial cells detect damage. In *C. elegans*, the skin is characterised by a rigid but flexible apical extracellular matrix (aECM), known as the cuticle, that surrounds a single syncytial epidermal layer (reviewed in (Sundaram and Pujol, 2024)). The cuticle surface contains circumferential-oriented furrows distributed periodically over the entire body length (Adams et al., 2023; Cox et al., 1981; McMahon et al., 2003). Embryos assemble the first larval cuticle, and then during each larval stage, a new cuticle is assembled, and the old one shed, in a process known as moulting (Lažetić and Fay, 2017). A transient precuticle is assembled to help to pattern the new cuticle and to shed the old one (Sundaram and Pujol, 2024).

The cuticle serves not only as a protective barrier against environmental insults but also as a dynamic interface that communicates crucial signals to the underlying epidermal tissue. We have previously described how cuticle damage triggers a series of responses in the epidermis. These responses can be set off by physical injury, infection with the fungus *Drechmeria coniospora*, or during the cyclic process of moulting. The organism's ability to mount a protective transcriptional response maintains tissue integrity to combat potential threats (Martineau et al., 2021; Pujol et al., 2008a; Sundaram and Pujol, 2024).

Mutants lacking periodic furrows have emerged as a valuable model for studying the interplay between cuticle integrity and epidermal immune activation. Mutations in any of the six furrow collagens (DPY-2, DPY-3, DPY-7, DPY-8, DPY-9, DPY-10) lead to the absence of periodic furrows in the cuticle (Cox et al., 1980; McMahon et al., 2003; Thein et al., 2003). We have previously shown that the same mutations exhibit a persistent immune activation (PIA), similar to the response triggered by moulting, physical injury or skin infection. This immune response involves the activation of the pivotal p38 MAPK/PMK-1 signalling pathway and the downstream SNF-12/SLC6 transporter and STAT-like transcription factor STA-2 (Dierking et al., 2011; Dodd et al., 2018; Pujol et al., 2008b). During infection or injury, the most upstream components known are the Damage Associated Molecular Pattern (DAMP) receptor DCAR-1, a GPCR, and the Gα protein GPA-12 (Zugasti et al., 2014). While loss of STA-2 or SNF-12 fully abrogates the induction of an immune response in furrow collagen mutants, inactivation of DCAR-1 only reduces it partially (Zugasti et al., 2014). We therefore proposed that a parallel mechanism must link the monitoring of furrow collagens' integrity to the activation of the immune response in the epidermis.

To gain deeper insights into how cuticle damage is sensed by the epidermis, we conducted a targeted genetic suppressor screen to identify genes acting downstream of furrow collagens and upstream of, or in parallel to, GPA-12. Notably, one suppressor identified in this screen harbours a mutation in the gene *spia-1* (*Suppressor of Persistent Immune*

Activation). This gene encodes a small nematode-specific secreted protein sharing a C-terminal domain with five other *C. elegans* proteins, including DPY-6, a mucin-type protein with a conserved role in cuticle deposition (Sun et al., 2022). The structured core of this common C-terminal domain (named CCD-aECM) is formed by conserved cysteine interactions predicted to allow potential homomeric and heteromeric interactions. Our expression and genetic analyses suggest that SPIA-1 functions as a secreted aECM protein, localised to the furrows, potentially relaying information about the state of the furrow collagens to the underlying epidermis.

Results & Discussion

Identification of *spia-1* as a suppressor of a constitutive immune response

We previously showed that wounding and infection of *C. elegans* trigger an immune response, characterised by the induction of the expression of the antimicrobial peptide (AMP) gene *nlp-29* in the epidermis (Couillault et al., 2004; Martineau et al., 2021; Pujol et al., 2008a; Taffoni et al., 2020; Zugasti et al., 2014). Interestingly, mutants in furrow collagens, which lack the organised circumferential furrow structure ("furrow-less mutants") (Aggad et al., 2023), also have a persistent immune activation (PIA) (Pujol et al., 2008b; Zugasti et al., 2014; Zugasti et al., 2016), in parallel to constitutively active detoxification and hyperosmotic responses (Dodd et al., 2018). The fact that these 3 responses are induced by the absence of furrows, yet differ in their signalling and effectors, led to the suggestion that a cuticle-associated damage sensor coordinates these 3 responses (Dodd et al., 2018).

To characterise this potential damage sensing mechanism, we conducted a genetic suppressor screen, designed to identify the upstream components of the pathway leading to the induction of the immune response in furrow-less mutants. The screen relies on the observation that a constitutively active form of GPA-12 (GPA-12gf) provokes a PIA by activating the p38/PMK-1 – STA-2 pathway, and on the use of a conditional promoter that is only active in the adult epidermis (Lee et al., 2018). In addition to a construct expressing GPA-12gf uniquely in the adult epidermis, the strain IG1389 we designed has the well-characterised *frIs7* transgene containing the *nlp-29* promoter driving GFP expression (*nlp-29*p::GFP) and a control DsRed transgene constitutively expressed in the epidermis, providing an internal control for the integrity of the epidermis and nonspecific transgene silencing (Pujol et al., 2008a). In the IG1389 strain, the *nlp-29*p::GFP reporter is not expressed in larvae but constitutively expressed in the adult, due to the expression of GPA-12gf ((Ziegler et al., 2009); Fig 1A). When any of the six furrow collagen genes, including *dpy-7*, is inactivated by RNAi in this strain, worms exhibit a high level of GFP at all developmental stages (green larvae-green adults) (Fig 1A, 1B and S1A). Inactivating any gene acting downstream of GPA-12, like *sta-2*, completely abolishes the expression of *nlp-29*p::GFP at all stages (red larvae-red adults; the so-called "no induction of peptide after infection" (Nipi) phenotype (Pujol et al., 2008a)) (Fig 1B and S1A). However, if the inactivated gene acts upstream of, or in parallel to, GPA-12, the expression of *nlp-29*p::GFP should be suppressed in larvae but reactivated by

114 GPA-12gf in the adult (Fig S1A), as observed with *dcar-1,* which acts upstream of *gpa-12* (Fig
115 1B).
116 We mutagenised the strain IG1389 using ethyl methanesulfonate (EMS), then
117 transferred synchronised F2 progeny onto *dpy-7* RNAi plates at the L1 stage and screened for
118 mutants that suppressed the PIA phenotype. Many mutants corresponded to genes acting
119 downstream of *gpa-12*, as they blocked the PIA at both larval and adult stages.
120 Complementation tests allowed us to identify new alleles of components of the known
121 pathway, including *snf-12(fr189)*. Interestingly, another subset of mutants had a phenotype
122 comparable to *dcar-1*, i.e the expression of *nlp-29*p::GFP was suppressed in larvae but
123 reactivated in the adult. Among them, the *fr179* mutant had the clearest phenotype (Fig 1B).
124 We called the *fr179* mutant *spia-1* (*Suppressor of Persistent Immune Activation).* We
125 confirmed that in the absence of *dpy-7* RNAi, *spia-1(fr179)* mutation also did not suppress the
126 *gpa-12*-induced PIA observed in adults, while *sta-2(ok1860)* completely abrogated it (Fig S1B).
127 This data suggested that *spia-1* does not act downstream of *gpa-12*. Moreover, unlike *dcar-1*
128 mutation, *spia-1(fr179)* still partly blocked the PIA in adults, when it is provoked by a
129 combination of *dpy-7* inactivation and *GPA-12gf* gain of function (Fig 1B). Together, these data
130 suggest that SPIA-1 acts in a partially non-redundant pathway parallel to GPA-12.
131 We backcrossed the *spia-1(fr179)* strain relying on the suppression of *nlp-29*p::GFP
132 induction upon *dpy-7* RNAi for the selection of *spia-1(fr179)* progeny. The underlying
133 molecular lesion was characterised by mapping through whole genome sequencing (WGS) of
134 a pool of backcrossed *spia-1(fr179)* independent recombinant mutants (Doitsidou et al., 2010;
135 Labed et al., 2012). The *spia-1(fr179)* worms carry a mutation in a splice donor site of the gene
136 *F09F9.2* (hereafter *spia-1*), predicted to result in a transcript with a frameshift and the
137 introduction of a premature stop codon leading to a truncated protein of 133 aa (Fig 1C). We
138 generated by CRISPR the allele *spia-1(syb7920)*, bearing a deletion of 710 bp in *spia-1* with a
139 modification of bp 789 (C -> T) to create a premature stop codon, and resulting in a truncated
140 SPIA-1 protein of 26 aa (Fig 1C). Results obtained with *spia-1(syb7920)* phenocopied those
141 obtained with *spia-1(fr179)* (Fig 1B and S1B). We further confirmed that the *spia-1*(*fr179)*
142 mutation abrogates the PIA phenotype produced by RNA inactivation of any of the six furrow
143 collagen genes (Fig 1D and S1C) but does not suppress the associated short size (i.e. the dumpy
144 phenotype; Fig S1D). Moreover, we confirmed that *spia-1* mutation in furrow-less mutants
145 reduced the endogenous expression of several AMPs genes including *nlp-29* (Fig S1E).
146 Interestingly, we did not observe reduced *gst-4* nor *gdph-1* expression (Fig S1E), which are
147 representative genes of the detoxification and osmotic stress responses kept in check by
148 furrow collagens (Dodd et al., 2018). These data indicate that SPIA-1 is specifically required in
149 the activation of the immune response upon furrow collagen loss.
150
151
152
153
154

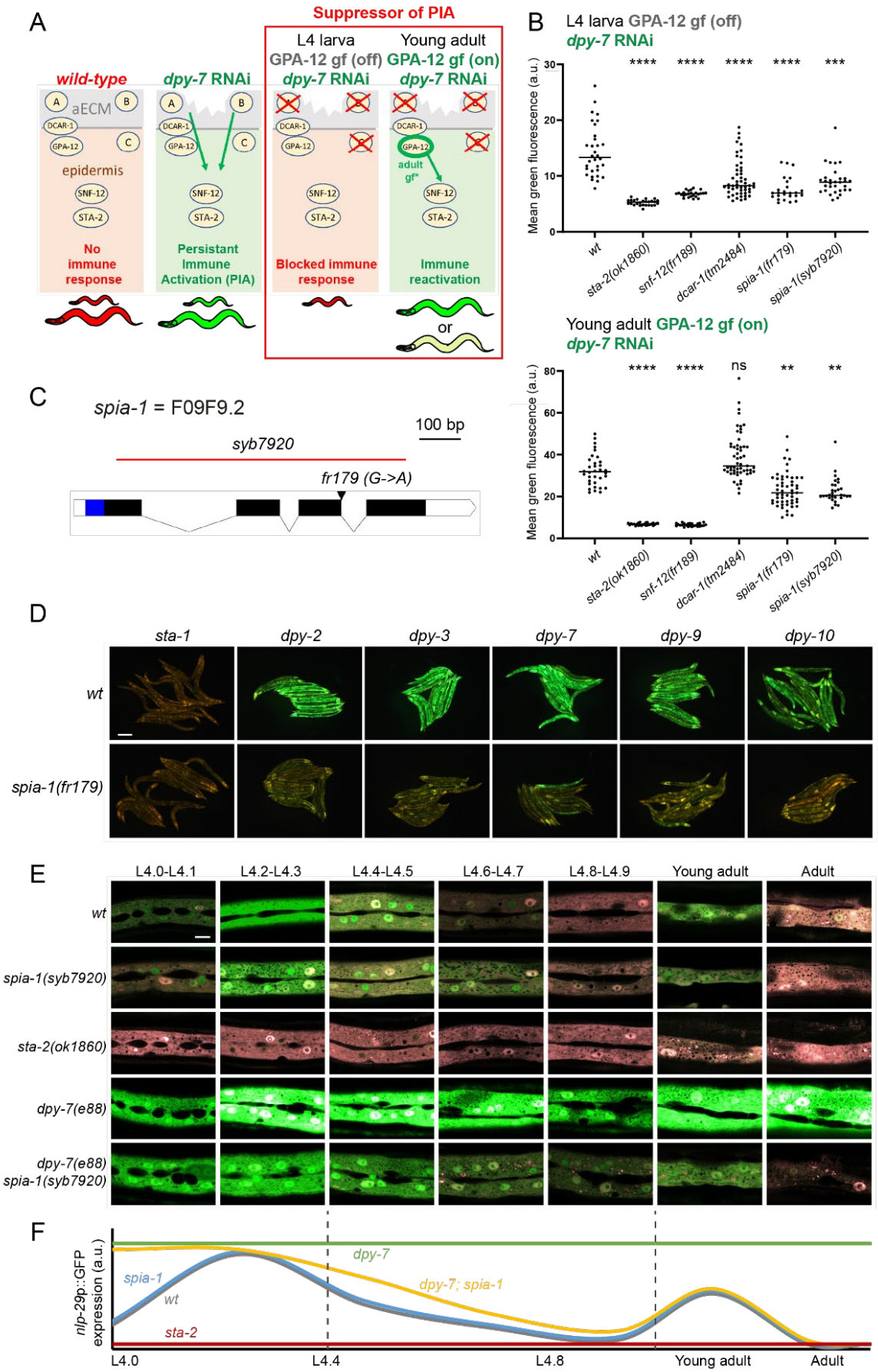

155 Fig 1. **Loss of *spia-1* suppresses furrow collagen AMP induction.**

(A) Design of the suppressor screen. The strain carries the *frIs7* transgene, containing an AMP transcriptional reporter (*nlp-29*p::GFP) and a control transgene (*col-12*p::DsRed) constitutively expressed in the epidermis. Under standard growth conditions, worms only express the control transgene and are red at all stages (left). RNAi inactivation of any furrow collagen gene, like *dpy-7*, leads to the expression of *nlp-29*p::GFP in a PMK-1/STA-2 dependent manner: worms appear "green" at all stages (middle). The strain used for the suppressor screen additionally bears the *frIs30* construct to express a gain of function of GPA-12 in the epidermis, only from the young adult stage (*col-19*p::GPA-12gf). In this strain, inactivation of a gene downstream of GPA-12 eliminates the expression of *nlp-29*p::GFP in both larvae and adults (Nipi phenotype (Pujol et al., 2008a)), whereas inactivation of any gene acting upstream of, or in parallel to, GPA-12, inhibits the expression of *nlp-29*p::GFP in the larvae but not in the adult due to the activation of GPA-12 (red larvae, green adults, right). This rescue is total if the targeted gene acts upstream of GPA-12 (A, *dcar-1*), but only partial if it acts in parallel to GPA-12 (B/C). (B) Quantification of the green fluorescence in worms carrying *frIs7* and *frIs30* constructs in different mutant backgrounds, upon *dpy-7* RNAi, in L4 and young adult stages (n>25). Statistics were made by comparing to the corresponding *wt* control; $^{**}p < 0.01$; $^{***}p < 0.001$; $^{****}p < 0.0001$. (C) Structure of the *spia-1* genomic locus. The location of the *fr179* mutation is indicated with an arrowhead, the extent of the *syb7920* deletion is shown with a red line. Exons are shown as black boxes, introns as solid lines. UTR are represented as white boxes; the blue region shows the sequence encoding the signal peptide of *spia-1*. (D) *spia-1(fr179)* suppresses the induction of *nlp-29*p::GFP in young adult worms after RNAi inactivation of furrow collagen genes. Wild-type and *spia-1(fr179)* mutants carrying the *frIs7* transgene were treated with the indicated RNAi bacteria, with *sta-1* used as a control (see Mat&Methods). Red and green fluorescences were visualised simultaneously in all images. Representative images of young adults from one of three experiments are shown; scale bar, 200 µm; see Fig S1C and S1D for quantification with the COPAS Biosort. (E) Oscillation of *nlp-29*p::GFP expression from L4 to adulthood. Representative confocal images of different mutant strains carrying the *frIs7* transgene, red and green fluorescences were visualised simultaneously. The L4 stage is subdivided into sub-stages with the shape of the vulva (Mok et al., 2015); n>5, scale bar, 10 µm. (F) Proposed schematic illustration of *nlp-29*p::GFP oscillation shown in E, units are arbitrary and not to scale.

In wild-type worms, *nlp-29* is expressed cyclically throughout development, possibly as a prophylactic protective mechanism following moulting (Aggad et al., 2023; Martineau et al., 2021; Sundaram and Pujol, 2024). We conducted a precise temporal analysis from the start of the L4 to the adult stage, using vulval shape as a proxy for developmental timing (Mok et al., 2015), as previously described (Aggad et al., 2023; Cohen et al., 2020). In the *nlp-29*p::GFP reporter strain, we observed a peak of GFP production at the L4.2-L4.3 and young adult stages (Fig 1E and 1F), suggesting a peak of *nlp-29* transcription a few hours before due to the folding time of GFP, which matches L3 & L4 moulting events respectively. A mutation in the transcription factor *sta-2* completely suppressed *nlp-29* induction, confirming that *sta-2* is required for the moulting-induced immune response (Fig 1E). In contrast, *spia-1(syb7920)* worms still presented both peaks and did not show any decrease in GFP production compared to wild-type worms (Fig 1E). In *dpy-7;spia-1(syb7920)* double mutants, although the PIA was reduced to levels qualitatively comparable to those in wild-type, as shown above, the moulting-induced peaks remained unaffected. Together, these results show that SPIA-1 is required in the furrow-less but not the moulting-induced immune responses.

200 *spia-1* encodes a secreted protein with a novel cysteine-cradle domain

201 *spia-1* is predicted to encode a secreted nematode-specific protein of 165 aa with no
202 previously known function (Davis et al., 2022). Its C-terminal region is annotated in the
203 Panther database with a signature PTHR37435 that has no associated function (Davis et al.,
204 2022; Thomas et al., 2022). This Panther family includes 5 other secreted *C. elegans* proteins:
205 DPY-6, a mucin-like protein with a conserved role in cuticle formation (Sun et al., 2022), and 4
206 other uncharacterised nematode-specific proteins: F01G10.9, F13B9.2, Y34B4A.10 and
207 F33D4.6 (Fig 2A). Orthologues of all 6 proteins are only present in nematodes, in free-living or
208 in parasitic forms, and found in different clades, like *Rhabditina*, *Tylenchina* and *Spirurina*.
209 These proteins have different lengths and contain regions with a compositional bias
210 suggesting they may be largely intrinsically disordered, their common and most conserved
211 part being located toward the C-terminus (Fig 2A and S2A). This common C-terminal region is
212 predicted by AlphaFold2 (Jumper et al., 2021) to adopt a globular structure composed of four
213 α-helices. These α-helices are arranged in two nearly orthogonal pairs, with two helices of one
214 pair packed at both edges of the other and thus creating a cradle-shaped domain. This globular
215 domain contains 4 invariant cysteines that define a sequence motif C_1-$(X)^{22}$-C_2-$(X)^7$-P-$(X)^3$-C_3-
216 $(X)^9$-C_4. The cysteine residues are predicted to form two disulfide bonds connecting the
217 α-helices, with C_1 bonding C_4 and C_2 bonding C_3 (Fig 2A, Sup movie). These disulfide bonds are
218 likely to play a structural role and be essential for the maintenance of the cradle-like shape of
219 the domain (Fig 2C and 2D). Owing to its features, this domain was named 'aECM cysteine-
220 cradle domain' (CCD-aECM or cysteine cradle domain) and its sequence diversity was added
221 to the Pfam database (Mistry et al., 2021) as a new entry PF23626.

222 The AlphaFold prediction of the cysteine cradle domain is in good agreement with
223 predictions obtained using secondary structure and disulfide bond prediction programs which
224 are based on different approaches (Buchan and Jones, 2019; Craig and Dombkowski, 2013;
225 Drozdetskiy et al., 2015). The multiple sequence alignment of the cysteine cradle domain
226 family (Fig 2D) or of the SPIA-1 orthologues in nematodes (Fig 2D) showed conserved features
227 that strongly support the predicted structural model. In addition to the 4 invariant cysteine
228 residues, these include: a highly conserved proline (Pro146 in SPIA-1) preceding and orienting
229 the α-helix 4, thus facilitating disulfide bond formation; two highly conserved
230 aspartate/asparagine (Asp129 & Asn137 in SPIA-1) at both caps of α-helix 2 needed for the
231 sharp turns of the polypeptide chain. In addition, hydrophobic interior interactions between
232 conserved aliphatic residues, as well as hydrogen bonds (e.g between Asn137 and the main-
233 chain N-atom of Trp133 in SPIA-1), probably stabilise the cysteine cradle domain. The residues
234 constituting the groove are also semi-conserved suggesting they may be important for
235 function (Fig 2B and 2D, Sup Movie). Moreover, aromatic residues line the groove: a
236 prominent tryptophan located on α-helix 2 (Trp133 in SPIA-1), a phenylalanine (Phe140 in
237 SPIA-1) and 3 tyrosines (Tyr121, Tyr125, Tyr144 in SPIA-1); they define a highly hydrophobic
238 interface that is probably involved in binding of unknown interaction partner(s). Interestingly,
239 in the AlphaFold2 model of Y34B4A.10 (uniprot ID:Q8WSP0), an N-terminal α-helix of the
240 protein itself docks into this groove (Fig 2E). A similar mode of interaction involving an α-helix

docked into a hydrophobic groove has been previously observed; for example, between the p53 transactivation domain α-helix and the MDM2 cleft (Kussie et al., 1996). Alternatively, aromatic hydrophobic residues are also known to engage in binding of proline-rich peptides (Cottee et al., 2013; Macias et al., 2002) suggesting another potential functional interaction in which the cysteine cradle domain might be involved (Fig 2F).

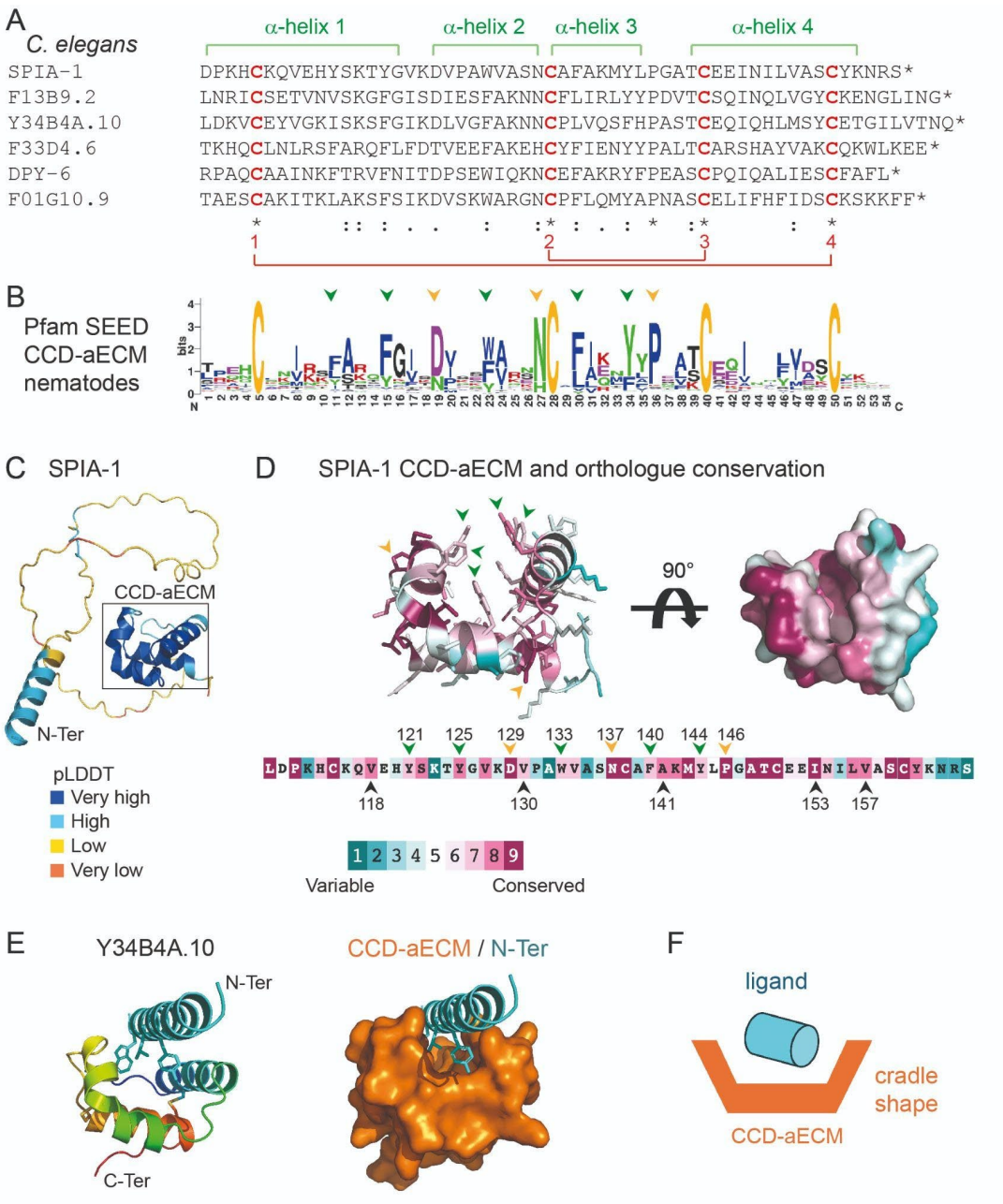

Fig 2. **SPIA-1 is a secreted protein containing a novel cysteine-cradle domain.**
(A) In *C. elegans*, 6 proteins share a common and previously uncharacterised domain in their C-terminal region, of which the amino acid sequences are depicted. This domain contains 4 invariant cysteine residues predicted to form two disulfide bridges (red) connecting 4 α-helices (green) and was named the cysteine cradle domain (CCD-aECM). (B) The sequence logo derived from the Pfam (PF23626) SEED alignment shows residues of the domain conserved across nematode homologues. The relative size of the residue letters indicates their frequency in the aligned sequences of the Pfam SEED. Arrows point to the aromatic residues lining the groove (green) and other

253 highly conserved amino acids (yellow). (C) SPIA-1 structural model predicted with AlphaFold2
254 (Abramson et al., 2024; Jumper et al., 2021), rendered in cartoon and coloured according to the
255 Predicted Local Distance Difference Test score (pLDDT), which indicates how well a predicted protein
256 structure matches protein data bank structure information and multiple sequence alignment data:
257 dark blue >90, light blue <90 & >70, yellow <70 & >50, orange <50. The CCD-aECM domain is framed
258 in black. (D) Amino acid sequence (bottom) and AlphaFold prediction of the CCD-aECM rendered in a
259 cartoon, with the side-chains shown as sticks (top left) or in surface with a 90° rotation (top right), and
260 coloured according to the Consurf conservation scores (Ashkenazy et al., 2016) based on SPIA-1
261 orthologs alignment. Arrows point to the aromatic residues lining the groove (green), aliphatic residues
262 that are in contact (black), and other highly conserved amino acids (yellow). Numbers indicate the
263 position of the amino acid in the full-length SPIA-1. The predicted structural model of SPIA-1 CCD-aECM
264 is also shown on Sup Movie. (E) The AlphaFold prediction model of Y34B4A.10 (left) is rendered in
265 cartoon and coloured in rainbow (blue to red indicating the path of the polypeptide chain from N- to
266 C-terminal end). Residues from the α-helix that are predicted to engage in hydrophobic interactions
267 are shown as sticks. The same model rendered in surface (right) demonstrates how the N-terminal α-
268 helix of Y34B4A.10 (cyan) is predicted to bind to the CCD-aECM groove of this protein (orange). (F)
269 Simplified illustration of the proposed model for the interaction of the CCD-aECM with a ligand.
270

271 ### *spia-1* is expressed in the epidermis and its expression oscillates during larval stages

272 During larval development, there are 4 moults spaced by ~7-8 hours during growth at
273 25°C. Genome-wide transcriptomic studies have revealed the rhythmic activity of thousands
274 of genes that align with the moulting cycle. They follow a repeated pattern of oscillations in
275 each cycle, peaking at a distinct point in each larval stage. A large proportion of the cycling
276 genes are expressed in the epidermis and are suggested to be required for the formation of
277 the new cuticle (Hendriks et al., 2014; Kim et al., 2013; Meeuse et al., 2020; Meeuse et al.,
278 2023; Tsiairis and Großhans, 2021). These oscillating transcripts include precuticle
279 components that are only transiently present when the new cuticle is synthesised at intermolt
280 and are endocytosed and degraded before each moult (Sundaram and Pujol, 2024). Analysing
281 the data from (Meeuse et al., 2020; Meeuse et al., 2023), we observed that the transcripts for
282 SPIA-1 and related proteins are part of these rhythmic oscillations (Fig 3A). We define that
283 each cycle ended by the expression of AMPs, including *nlp-29*, which have been proposed to
284 be induced to protect the epidermis while the old cuticle is shed (Martineau et al., 2021), and
285 that one of the first genes to start to oscillate in the early L1 is *dpy-6*. It encodes a protein that,
286 in addition to its CCD-aECM, is enriched with tandem repeats of serine and threonine residues
287 similar to those found in highly glycosylated mucins (Sun et al., 2022). We then reanalysed the
288 peak phase of genes that are known to be important for cuticle morphogenesis relative to
289 *dpy-6*. All 5 genes encoding a CCD-aECM peak just after the pre-cuticle genes (orange) *let-653*
290 and *fbn-1,* with *F01G10.9* (green) peaking together with the pre-cuticle genes *noah-1/2* & *lpr-3*
291 and the 6 furrow Dpy collagens *dpy-2, dpy-3, dpy-7, dpy-8, dpy-9, dpy-10* (brown), followed by
292 *spia-1, F13B9.2*, *F33D4.6* and *Y34B4A.10* (blue). These are then followed by the non-furrow
293 collagens like *dpy-4, -5, -13* (black), and then the AMPs (pink) at the very end of each cycle (Fig
294 3B). The observation that CCD-aECM encoding genes cycle at the beginning of the new cuticle

295 synthesis, together with precuticle and furrow collagen genes suggest a role in the formation
296 of the new cuticle, including a very early role for *dpy-6*.

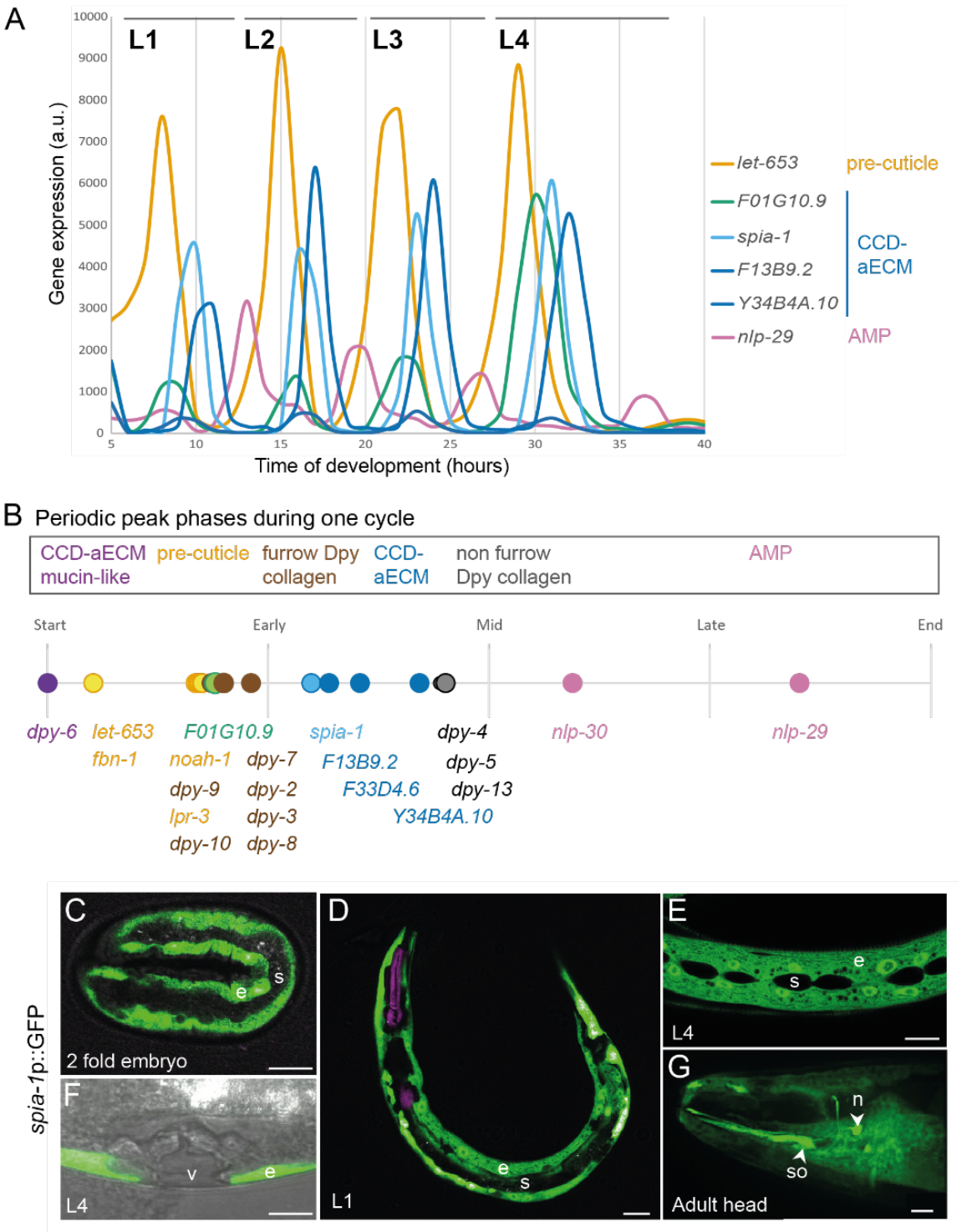

297 Fig 3. ***spia-1* is expressed in the epidermis and oscillatory between each moult.**
298 (A) AMP and aECM gene expression oscillates between each moult, absolute levels of expression data from
299 (Meeuse *et al.* 2020). (B) Between each moult, a timeline of gene expression is represented, with *dpy-6* starting
300 each cycle. Data adapted from (Meeuse *et al.* 2020). (C-G) Expression pattern of *spia-1* transcript in worms
301 carrying the *frEx631[pSO22(spia-1*p::GFP*), myo-2*p::mCherry*]* transgene. Representative confocal images, n>5,
302 of (C) 2-fold embryo, (D) L1 larva, (E, F) L4 larva, and (G) adult head. The signal is visible in the epidermis (e) at all

303 stages, and also in head socket cell (so) and a neuron (n), but not in the seam cell (s), nor the vulva (v). Grey
304 colour in (F) was acquired with a transmitted detection module; scale bar, 10 µm.
305
306 Targeted DamID studies are consistent with SPIA-1 expression in the epidermis hyp7
307 in larval stages (Katsanos et al., 2021). In adult-specific single cell RNAseq, *spia-1* is also found
308 expressed in cephalic and inner labial socket and phasmid sheath cells (Ghaddar et al., 2023).
309 A transcriptional reporter confirmed that *spia-1* is expressed in the main epidermal cell and
310 socket cells but is not visible in other epithelial cells like the seam cells, nor in the vulval cells
311 (Fig 3C-G). The expression starts in embryos at the 2-fold stage, which is the time when pre-
312 cuticle components like LPR-3 start to mark the cuticle, but later than the earliest components
313 of the pre-cuticle sheath like NOAH-1 and FBN-1 (Fig 3C) (Balasubramaniam et al., 2023;
314 Birnbaum et al., 2023; Cohen and Sundaram, 2020; Vuong-Brender et al., 2017). The
315 transcriptional reporter might be missing some of the endogenous regulation, but it includes
316 1.2 kb of upstream genomic sequence that harbours several predicted binding motifs for
317 transcription factors, including NHR-23 that is important for oscillatory gene expression in
318 epithelial cells (Davis et al., 2022; Gerstein et al., 2010; Johnson et al., 2023). Taken together
319 these observations suggest that *spia-1* is expressed in epidermal cells and oscillates with a
320 peak phase that follows the six furrow collagens and precuticle components.
321
322 SPIA-1 is localised to aECM periodic furrows
323 We tagged the SPIA-1 protein by insertion of GFP in 3 different positions: at the N-
324 terminus after the signal peptide, at the C-terminus before the stop codon, or internally before
325 the CCD-aECM. We introduced extra-chromosomal transgenes expressing these GFP-tagged
326 SPIA-1 under the control of its own promoter into the *spia-1(syb7920)* mutant. Upon RNAi
327 inactivation of *dpy-7*, the *spia-1(syb7920)* mutation suppressed the PIA phenotype; among the
328 three transgenes, only the one containing the internally tagged SPIA-1::sfGFP (hereafter SPIA-
329 1::sfGFP-int) rescued the PIA phenotype (Fig 4B and 4C). This is consistent with the lack of
330 observable GFP signal in either of the 2 other strains. In contrast, the functional protein SPIA-
331 1::sfGFP-int was visible in association with cuticle furrows starting in late embryonic stages
332 and continuing throughout all larval stages (Fig 4D). We further generated a knock-in strain,
333 IG2212, with SPIA-1 tagged with mNeonGreen (mNG) at the same position as the internal
334 sfGFP. We confirmed that SPIA-1::mNG was located at furrows as it colocalised with DPY-
335 2::BFP (Fig S3B). In both strains, SPIA-1 was still present in the adult, but more faintly (Fig 4D
336 and S3A). We could not detect it in the shed cuticle, but this could be due to its low signal. In
337 addition, SPIA-1 accumulated in the vulva lumen during the mid-L4 stage (Fig 4D). In
338 accordance with its cyclic expression, the fluorescence intensity of furrow-associated SPIA-1
339 also cycled, peaking in the middle of the L4 larval stage (Fig 4E). SPIA-1 strongly accumulated
340 in vesicles preceding each moult, like precuticular components. During the L4 larval stage, the
341 precuticular lipocalin LPR-3 was shown to be only transiently present, being secreted from the
342 L4.3 stage onwards, and observed in an annular pattern between L4.4 to L4.7 (Forman-
343 Rubinsky et al., 2017; Katz et al., 2022). Using vulval shape as a proxy for developmental

344 timing, as described previously, we observed that in a double labelled mCherry::LPR-3,
345 SPIA-1::sfGFP-int strain, SPIA-1 started to be visible at the L4.4 stage, at furrows in a pattern
346 complementary to LPR-3, and in fluorescent vesicles (Fig 4E). Its level at the furrows then
347 decreased, while it remained in vesicles throughout the end of the L4 stage.
348 The intermolt peak and strong accumulation of SPIA-1 in vesicles before moulting
349 resembled that of precuticular components like LPR-3 (Birnbaum et al., 2023; Forman-
350 Rubinsky et al., 2017). Furthermore, we saw that SPIA-1::sfGFP-int and mCherry::LPR-3
351 vesicles partly overlapped (Fig 4E). To study further the nature of the SPIA-1 transient
352 fluorescent vesicles, we combined SPIA-1::mNG with the lysosomal hydrolase
353 NUC-1::mCherry that served as an endosomal and a lysosomal reporter, as previously
354 described (Miao et al., 2020) and the DPY-2::BFP reporter to mark the furrows. Interestingly,
355 in early L4, while NUC-1, SPIA-1 and DPY-2 are each visible in fluorescent vesicles, most of
356 these were independent (Fig 4F). This suggests that SPIA-1 and DPY-2 are initially not
357 associated with the same trafficking compartments, even though they colocalise at furrows
358 once secreted in the matrix, and might be secreted in different ways. Remarkably, in late L4,
359 most SPIA-1::mNG and NUC-1 fluorescent vesicles adopted a tubular structure, characteristic
360 of lysosomal compartments, and appeared mostly colocalised (Fig 4F). It is interesting to note
361 that these lysosomal tubular structures are visible with the mNG but not sfGFP tagged SPIA-1
362 strain, which presumably reflect the quenching of the latter's fluorescence in acidic
363 compartments. Overall, these data suggest that, in late L4, SPIA-1 is directed to lysosomes for
364 degradation, a mark of precuticular components. This is also consistent with its reduced
365 presence at furrows at the adult stage.
366 Altogether, these data suggest that SPIA-1 is an atypical cuticle component that shares
367 some temporal and trafficking features of pre-cuticle, where its matrix signal peaks in the
368 intermolt period of cuticle synthesis, after which most of it is cleared by endocytosis.
369 Interestingly, the secreted hedgehog-related protein GRL-7, one of the few known
370 components to be specifically positioned at the furrows in the pre-cuticle, contains a ground-
371 like nematode-specific domain, which is another type of cysteine domain. It has been
372 suggested to have a signalling role related to matrix association (Chiyoda et al., 2021; Serra et
373 al., 2024; Sundaram and Pujol, 2024).
374

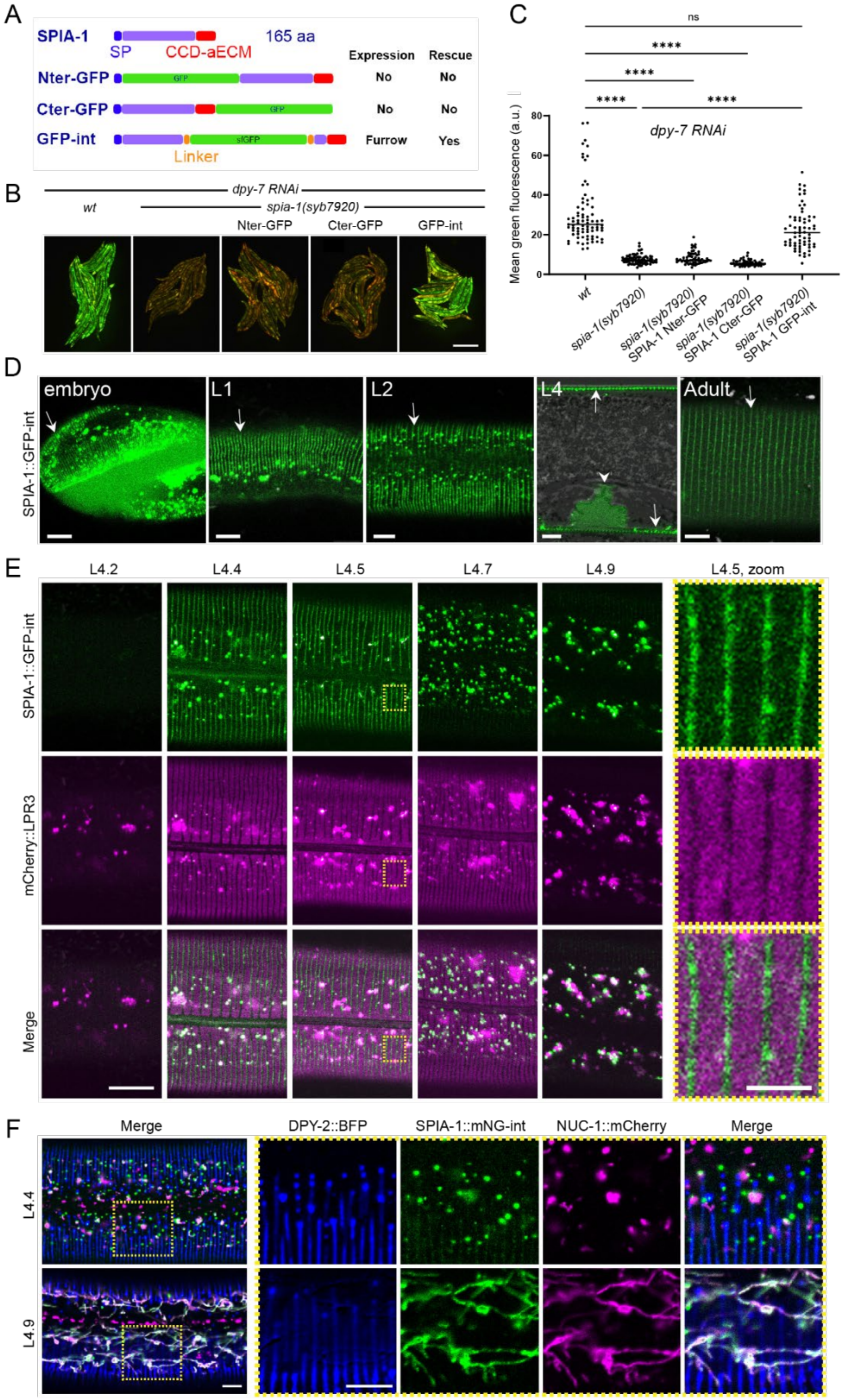

Fig 4. **SPIA-1 localises to furrows.**

(A) Position of the insertion of GFP in each translational reporter with their expression pattern and rescue activities. For the KI strain, mNG is inserted at the same place as in GFP-int. (B-C) *spia-1* mutation suppresses *nlp-29*p::GFP overexpression in *dpy-7* worms. The rescue of this suppression has been tested in *spia-1(syb7920)* young adults with the extra-chromosomal gene producing SPIA-1 tagged with GFP in Nter, Cter or internal

position, in three independent experiments. (B) Representative images of one experiment; scale bar, 500 µm. (C) Relative green fluorescence is quantified (n=58-79); ****$p < 0.0001$. (D) Representative confocal images of the SPIA-1::sfGFP reporter (GFP-int) in 3-fold embryo, L1, L2, L4 vulval lumen and adult. We used a laser power ~2 times higher in adults compared to other stages (see Fig S3A). White arrows and arrowhead indicate signal in furrows and in vulval lumen, respectively; n>5, scale bar, 5 µm. (E) The L4 stage is subdivided into sub-stages in relation to the shape of the vulva, as previously described (Mok et al., 2015). SPIA-1::sfGFP and mCherry::LPR-3 are observed in parallel. ~7 times magnification of the areas contained in the dashed rectangles are provided on the far right; scale bar, 10 µm (left), 2 µm (magnified area). (F) Representative confocal images of L4.4 (top) and L4.9 (bottom) larvae expressing DPY-2::BFP, SPIA-1::mNG-int, and NUC-1::mCherry. ~2.5 times magnification of the areas contained in the dashed rectangles are provided on the far right. Both single channels and the merge are shown; n>5, scale bar, 5 µm.

SPIA-1 acts downstream of furrow collagens

spia-1 was identified as a suppressor of the persistent immune activation provoked by the absence of furrows. Although *spia-1* did not reverse the Dpy phenotype of furrow-less mutants, it conceivably exerted its suppressive function by restoring normal furrow morphology. We examined the cuticle of worms deficient for different furrow collagens in the *spia-1(fr179)* background, with a COL-19::GFP marker and a DPY-7::sfGFP marker. In no case did the *spia-1* mutation restore furrows (Fig 5A and 5B). We noticed that when furrows are absent in a *dpy-2* mutant, the precuticle component LPR-3 cannot assemble anymore in its specific anti-furrow pattern during the mid L4, as visualised with sfGFP::LPR-3. The absence of *spia-1* could not restore the correct LPR-3 localisation in furrow-less mutants (Fig 5C). The absence of *spia-1* did not affect cuticle collagen DPY-7 or COL-19 nor precuticle LPR-3 localisation in an otherwise wild-type background (Fig 5A-C). Together, these observations indicate that *spia-1* acts downstream of the patterning and signalling roles of the furrow collagens.

We then investigated SPIA-1 localisation in a furrow-less context, either in a *dpy-2* mutant or by RNAi inactivation of *dpy-7* (Fig 5D and S4). Furrow-less mutant conserved the vesicular and tubular pattern of SPIA-1 in L4 in the epidermis, and SPIA-1 was still present in the cuticle, suggesting that SPIA-1 was correctly produced, transported and degraded. However, in both L4 and adult, the furrowed pattern of SPIA-1 was lost and replaced by a signal randomly distributed in the cuticle (Fig 5D). We confirmed that the inactivation of any of the 6 furrow collagens, here *dpy-3*, impacts the localisation of other furrow collagens in the cuticle (Fig 5B) (McMahon et al., 2003). Thus, SPIA-1, like LPR-3, requires the presence of furrow collagens in the cuticle for its proper matrix localisation.

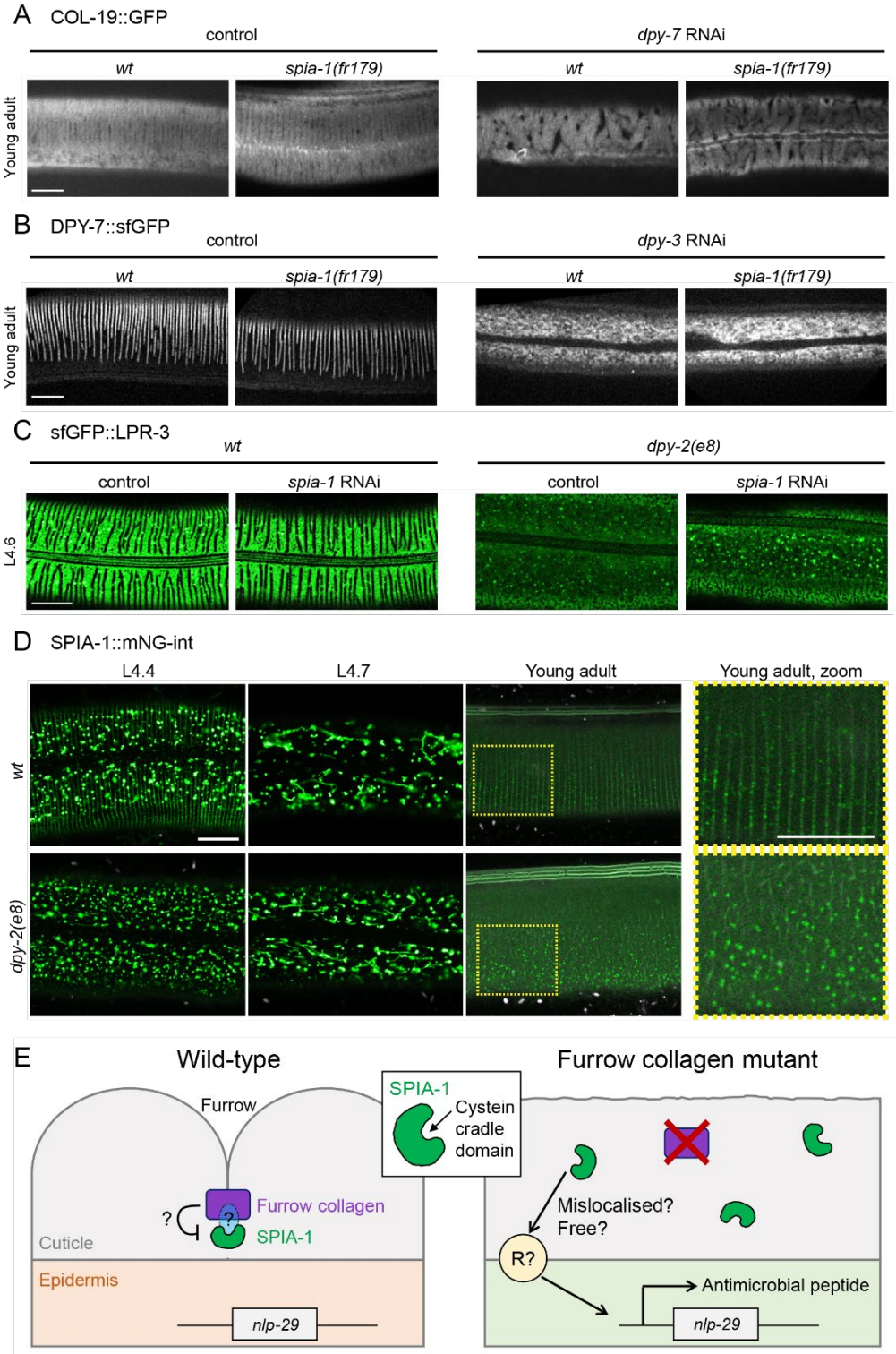

Fig 5. **SPIA-1 acts downstream of furrow collagens.**
(A) *spia-1(fr179)* does not suppress COL-19::GFP abnormal pattern following *dpy-7* RNAi. Representative images of *wt* or *spia-1(fr179)* young adults carrying COL-19::GFP treated with *sta-1* or *dpy-7* RNAi bacteria; n>5, scale bar, 10 µm. (B) *spia-1* does not suppress the absence of furrows following *dpy-3* RNAi; representative images of *wt* or *spia-1(fr179)* worms carrying DPY-7::sfGFP treated with *sta-1* or *dpy-3* RNAi bacteria; scale bar, 10 µm. (C) *spia-1* does not suppress the abnormal sfGFP::LPR-3 in *dpy-2(e8)*; representative images of *wt* or *dpy-2(e8)* L4.6 worms carrying sfGFP::LPR-3 treated with control (*sta-1)* or *spia-1* RNAi bacteria; scale bar, 10 µm. (D)

SPIA-1::mNG-int is mislocalised in *dpy-2(e8)* mutants. Representative images of *wt* or *dpy-2(e8)* L4.4, L4.7, or young adult worms carrying SPIA-1::mNG-int. We used a laser power ~2 times higher in adults compared to other stages, see Fig S3A. A ~2.5 times magnification of the areas contained in the dashed rectangles is provided on the far right; n>5, scale bar, 10 µm. (E) Cartoon presenting the proposed model for SPIA-1 activity in wild-type or furrow-less adults. Not to scale.

A model for the role of SPIA-1 and its novel CCD-aECM domain

We propose a dual role of SPIA-1 as an atypical precuticular component of the furrow, as well as a cuticular sensor of cuticle damage. SPIA-1 shares characteristics of precuticular components as it is present at intermolt and highly endocytosed and degraded in lysosome before moulting. But unlike other characterised precuticular components, SPIA-1 is still present in the adult cuticle. Precuticular and some cyclic cuticular components like furrow collagens, are suggested to have a role in patterning the new cuticle ((Aggad et al., 2023; Forman-Rubinsky et al., 2017; Sundaram and Pujol, 2024), Fig 5A-C). In the absence of SPIA-1, we observed no obvious phenotype associated with cuticle morphogenesis, nor in patterning the precuticle LPR-3 or furrow collagens. Although this could mean that it has no role in cuticle morphogenesis, SPIA-1 could act redundantly, potentially with other cysteine cradle domain proteins. All the cysteine cradle domain proteins including SPIA-1 are only found in nematodes and predicted to be secreted. They are encoded by genes that have a cyclic expression and are predicted or already demonstrated to be expressed in the epidermis (Davis et al., 2022; Ghaddar et al., 2023; Katsanos et al., 2021; Meeuse et al., 2023). Altogether, these strongly suggest that all 6 cysteine cradle domain proteins are matrix proteins of the specialised nematode cuticle, hence the name of CCD-aECM for this novel Pfam domain.

SPIA-1 is required for the immune response provoked by the loss of furrows. In furrow-less mutants, we showed that SPIA-1 is aberrantly localised in the cuticle. The mislocalisation of SPIA-1 could trigger the persistent immune response in the epidermis. In normal circumstances, SPIA-1 could be muted by being directly or indirectly bound to collagen, thereby preventing it from signalling damage. In the absence of furrow collagen, it would be free to interact with unknown components, in parallel to the DCAR-1/GPA-12 pathway, to activate an immune response (Fig 5E). One hypothesis is that SPIA-1 could be directly linked to furrow collagens via its CCD-aECM. While 4 of the CCD-aECM proteins have not been studied yet, it is interesting to report that when endogenously tagged with mNG, DPY-6 is observed at furrows in the cuticle (Fig S5). Further investigations would be required to understand the potential role for CCD-aECM proteins in building a functional aECM and monitoring cuticle integrity.

Materials and Methods

EMS suppressor screen and mutation identification

P0 from the strain IG1389 *frIs7[nlp-29*p::GFP*, col-12*p::DsRed*] IV; frIs30[(col-19p::GPA-12gf), pNP21(pBunc-53::GFP)]* were mutagenised with EMS as previously described (Labed et al.,

471 2012; Pujol et al., 2008a). Individual synchronised F2 L1 worms were plated on *dpy-7* RNAi
472 plates. Late larval F2 that showed a low expression of *nlp-29*p::GFP were cloned. The ones that
473 then showed a higher GFP expression at adult stage were further analysed. As a positive
474 control for the mutagenesis, several candidates that still abrogate the GFP signal at the adult
475 stage were also cloned, and led to the isolation of several new Nipi alleles including
476 *snf-12(fr189)*. *spia-1* was further backcrossed with IG274 *frIs7* and a dozen of F2 without the
477 GPA-12gf were isolated, then pooled to send their genome to sequencing (BGI). Sequences
478 were analysed with MiModD v0.1.9, https://mimodd.readthedocs.io/en/latest, based on
479 CloudMap (Minevich et al., 2012), using the sub-commands *varcall*, then *varextract* and finally
480 *annotate*. This later step required SnpEff v5 and the SnpEff database *WBcel235.86*. The VCF
481 file produced was re-formatted using a Python script to allow the curation of all putative
482 mutations with user-defined thresholds.
483

484 ## Nematode strains

485 All *C. elegans* strains were maintained on nematode growth medium (NGM) and fed with *E.*
486 *coli* OP50, as described (Stiernagle, 2006). Table S1A shows a list of the strains used in this
487 study, including those previously published: BE93 *dpy-2(e8) II* (Cox et al., 1980), IG1060
488 *sta-2(ok1860) V; frIs7[nlp-29p::GFP, col-12p::DsRed] IV* (Dierking et al., 2011), IG1689
489 *dpy-7(e88) X; frIs7[nlp-29p::GFP, col-12p::DsRed] IV* (Dodd et al., 2018), UP3666
490 *lpr-3(cs250[ssSfGFP::LPR-3]) X* & UP3808 *lpr-3(cs266[mCherry::LPR-3]) X* (Forman-Rubinsky et
491 al., 2017), IG1389 *frIs7[nlp-29p::GFP, col-12p::DsRed] IV; frIs30[(col-19p::GPA-12gf),*
492 *pNP21(pBunc-53::GFP)] I* & IG1392 *sta-2(ok1860) V; frIs7[nlp-29p::GFP, col-12p::DsRed] IV;*
493 *frIs30[(col-19p::GPA-12gf), pNP21(pBunc-53::GFP)] I* (Lee et al., 2018), XW18042
494 *qxSi722[dpy-7p::DPY-7::sfGFP] II* & XW5399 *qxIs257[ced-1p::NUC-1::mCHERRY, unc-76(+)] V*
495 (Miao et al., 2020), IG274 *frIs7[col-12p::DsRed, nlp-29p::GFP] IV; fln-2(ot611) X* (Pujol et al.,
496 2008a), TP12 *kaIs12[COL-19::GFP]* (Thein et al., 2003), IG1426 *dcar-1(tm2484) V;*
497 *frIs7[nlp-29p::GFP, col-12p::DsRed] IV; frIs30[(col-19p::GPA-12gf), pNP21(pBunc-53::GFP)] I*
498 (Zugasti et al., 2014) and HW1371 *xeSi137[F33D4.6p:: gfp::h2b::pest::unc-54 3'UTR; unc-119*
499 *+] I* (Meeuse et al., 2023). Strains with extrachromosomal hygromycin resistance genes were
500 selected on NGM plates supplemented with 0.3 mg/ml hygromycin B (Sigma-Aldrich).
501

502 ## Constructs and transgenic lines

503 All following constructs were made using SLiCE (Motohashi, 2015) and the plasmid editor Ape
504 (Davis and Jorgensen, 2022) and all primer sequences used to generate specific PCR amplicons
505 are in Table S1B. A transcriptional construct (pSO22), was generated by cloning a PCR amplicon
506 (3321-3322) containing 1.23 kb upstream of the *spia-1* start codon into pPD95.75 (Fire et al.,
507 1990). To create translational constructs, GFP was inserted in *spia-1* either at the C-terminal
508 ends (pSO24: 3326-3327) or after the N-terminal signal peptide (pSO25: 3366-3367, 2093-
509 3365). Internal tag translational construct (pSO26) was generated by inserting the sfGFP
510 (kindly provided by A. Golden and H. Smith) in SPIA-1 at position 92 flanked with N-tag and C-

511 tag linker used in pMLS288 and pMLS287 respectively (Schwartz and Jorgensen, 2016) (3392-
512 3393, 3394-3395).
513 pSO22 was injected at the concentration of 50 ng/µl with the co-injection marker
514 *ttx-3*p::RFP at 50 ng/µl into N2 to get IG1986 and the co-injection marker *myo-2*p::mCherry at
515 2 ng/µl into N2 to get IG1988. Translational constructs (pSO24, pSO25, or pSO26) were
516 injected at the concentration of 2 ng/µl, with the co-injection marker *myo-2*p::mCherry at 2
517 ng/µl and the HygR selection plasmid pZX13 at 50 ng/µl with pKS at 50 ng/µl into N2 (pSO24
518 and pSO25), or IG2093 *spia-1(fr179)* (pSO26) to get IG1999, IG2062, IG2108 respectively.
519 The strain PHX7920 *spia-1(syb7920)* generated by CRISPR editing (SunyBiotech), has a
520 deletion of 710 bp (bp 79-788) in *spia-1* and a modification of bp 78 (C -> **T**) to create a
521 premature stop codon. The sequence from the **ATG** to the original **stop** codon is
522 ATGAAGCTAGTTGTTGTTTTGGCTTGTCTTGTTGTAGTAGCTGAGGCTTATTCAAAATCTGGAAATCC
523 ATACAAGACT**T**AACTTGTGAGGAGATTAACATTTTGGTGGCCTCTTGCTACAAGAACAGAAGC**TAA**,
524 resulting in a truncated SPIA-1 protein of 26 aa. All the transgenic strains carrying *spia-1(fr179)*
525 or *spia-1(syb7920)* were obtained by conventional crosses and genotypes were confirmed by
526 sequencing (see Table S1A for a list of all strains).
527 The strain IG2212 *spia-1(fr201(SPIA-1internal mNG^SEC^::3xFLAG))* was generated by
528 CRISPR editing using a self-excising cassette as previously described (Dickinson et al., 2015);
529 *mNG^SEC^::3xFLAG* was inserted at the same position than the GFP in pSO26. A repair
530 template was constructed using Gibson cloning to insert a 622 bp 5' homology arm and a 575
531 bp 3' homology arm into an *Avr*II+*Spe*I digested pDD268 backbone (Dickinson et al., 2015) to
532 make pJW2521. A sgRNA vector (pJW2568) targeting the ATCGGAAACAGTTGGTGGAG TGG
533 sequence (PAM underlined, not included in vector) was made through SapTrap (Schwartz and
534 Jorgensen, 2016), by cloning of an annealed oligo pair into pJW1839. Wild-type N2 animals
535 were injected with pJW2568, pJW2521, a pCFJ2474 Cas9 plasmid, a *mlc-1*p::mNG co-injection
536 marker (pSEM229), and a *snt-1*p::HisCl (pSEM238) counter selection marker (Aljohani et al.,
537 2020; El Mouridi et al., 2020; El Mouridi et al., 2021). Plates were flooded with hygromycin
538 and histamine as previously described (Dickinson et al., 2015). A hygromycin-resistant, rolling
539 strain [JDW774 *spia-1((spia-1(spia-1 internal mNG^SEC^::3xFLAG)) X*] was recovered and then
540 the self-excising cassette was removed through heat-shock as described in (Dickinson et al.,
541 2015) to create IG2212. The strain MCP597 *dpy-2(bab597[DPY-2::mTaqBFP2]) II* was obtained
542 by Segicel, by adding BFP at the C-terminus of DPY-2. The strain PHX3742
543 *dpy-6(syb3742(DPY-6::mNG))* was obtained by SunyBiotech, by adding mNG at the C-terminus
544 of DPY-6. All knock-in strains were confirmed by PCR genotyping using primers outside the
545 homology arms and Sanger sequencing.
546

547 ## Sequence analyses

548 The following *C. elegans* CCD-aECM proteins (WormBase geneID/UniProt ID) SPIA-1/Q19281,
549 Y34B4A.10/Q8WSP0, F33D4.6/O44189 (long isoform with the CCD-aECM), DPY-6/Q94185,
550 F01G10.9/O17767 and F13B9.2/Q19385, were analysed with BlastP (Altschul et al., 1990),
551 WormBase (Davis et al., 2022), Panther (Thomas et al., 2022), Pfam (Mistry et al., 2021),

552 Interpro (Paysan-Lafosse et al., 2023) and AlphaFold2 & 3 (Abramson et al., 2024; Jumper et
553 al., 2021). We built the Pfam family PF23626 (named 'aECM cysteine-cradle domain') using
554 sequences of CCD-aECM paralogues with domain boundaries defined based on the AlphaFold2
555 prediction models; Pfam PF23626 will be available in Pfam release 37.1. We iteratively
556 searched for homologues using the HMMER package (Potter et al., 2018) and used an inclusion
557 threshold of 27 bits. SPIA-1 orthologues including PIC17963.1 [*Caenorhabditis nigoni*],
558 CAI5454296.1 [*Caenorhabditis angaria*], WKY17175.1 [*Nippostrongylus brasiliensis*],
559 VDO70284.1 [*Heligmosomoides polygyrus*], EPB77628.1 [*Ancylostoma ceylanicum*],
560 CDJ96309.1 [*Haemonchus contortus*], XP_013305412.2 [*Necator americanus*], KAF8381298.1
561 [*Pristionchus pacificus*], KAK5976273.1 [*Trichostrongylus colubriformis*], KAI6173309.1
562 [*Aphelenchoides besseyi*] were used for alignment and Consurf conservation scores
563 (Ashkenazy et al., 2016).
564

565 ### RNA interference

566 RNAi bacterial clones were obtained from the Ahringer library (Kamath et al., 2003) and
567 verified by sequencing (see Table S1C). RNAi bacteria were seeded on NGM plates
568 supplemented with 100 g/ml ampicillin and 1 mM Isopropyl-β-D-thiogalactopyranoside
569 (IPTG). Worms were transferred onto RNAi plates as L1 larvae and cultured at 25 °C until L4 or
570 young adult stage. In all our experiments, we use *sta-1* as a control, as we have shown over
571 the last decade that it does not affect the development nor any stress or innate response in
572 the epidermis (Dierking et al., 2011; Lee et al., 2018; Taffoni et al., 2020; Zhang et al., 2021;
573 Zugasti et al., 2014).
574

575 ### *nlp-29*p::GFP fluorescent reporter analyses

576 Representative fluorescent images including both green (*nlp-29*p::GFP) and red (*col-*
577 *12*p::DsRed) fluorescence were taken of *frIs7* transgenic worms mounted on a 2% agarose pad
578 on a glass slide, anaesthetised with 1 mM levamisole in 50 mM NaCl, using the Zeiss AxioCam
579 HR digital colour camera and AxioVision Rel. 4.6 software (Carl Zeiss AG). For quantification,
580 the same worms were manually isolated and imaged again. Each worm was computationally
581 contoured on ImageJ, by successively applying the RenyiEntropy threshold method provided
582 by the plugin CLIJ2 (Haase et al., 2020) to the red image, converting the grayscale image to
583 binary, suppressing noise (binary open), filling holes, and creating masks (analyze particles).
584 Masks were applied to the original images, systematically controlled by eye, and corrected if
585 needed. Mean green fluorescence signal was further measured for each contoured worm.
586 In figures S1C and S1D, *nlp-29*p::GFP expression was quantified with the COPAS Biosort (Union
587 Biometrica; Holliston, MA) as described in (Labed et al., 2012). In each case, the results are
588 representative of at least three independent experiments with more than 70 worms analysed.
589 The ratio between GFP intensity and size (time of flight) is represented in arbitrary units.
590
591
592

593 ## Confocal microscopy
594 Worms were mounted on a 2 % agarose pad, in a drop of 1 mM levamisole in 50 mM NaCl.
595 Images were acquired during the following 60 min, using Zeiss confocal laser scanning
596 microscopes (LSM780, 880 or 980) and the acquisition software Zen with a Plan-Apochromat
597 Oil DIC M27 40×/1.4 or 63×/1.40 objective. Pinhole size was set to 1 AU. Samples were
598 illuminated with 405 nm (BFP), 488 nm (GFP, mNG) and 561 nm (mCherry) with varied laser
599 power based on protein abundance and tissue imaged, with 4 lines accumulation and 750 gain
600 settings. Spectral imaging combined with linear unmixing was used to separate the
601 autofluorescence of the cuticle.
602
603 ## Quantitative PCR
604 Total RNA samples were obtained by Trizol (Invitrogen)/chloroform extraction. One mg of
605 total RNA was then used for reverse transcription (Applied Biosystems). Quantitative real-time
606 PCR was performed using 1 µl of cDNA in 10 µl of SYBR Green (Applied Biosystem) and 0.1 mM
607 of primers on a 7500 Fast Real-Time PCR System using *act-1* as a reference gene. Primer
608 sequences are provided in supplementary Table S1B.
609
610 ## Statistical analysis
611 Data were analysed with the GraphPad Prism 10.3 software. Statistical differences between
612 groups were determined by the Kruskal-Wallis' test followed by the Dunn's test. Data were
613 considered significantly different when *p*-value was less than 0.05.
614
615 ## Acknowledgements
616 We thank Damien Courtine for the installation and use of MiModD, Ebrima Bojang and Sarah
617 Sharkaoui for participation in the genetic screen that identified *spia-1*, Matt Ragle, Emma
618 Cadena, Jack Clancy for cloning and injections, Mathieu Fallet for help in image
619 quantifications. We thank Andy Golden and Harold Smith for sending us the sfGFP plasmid,
620 Margaux Gibert and SEGiCel (SFR Santé Lyon Est CNRS UAR 3453, Lyon, France) for the DPY-
621 2::BFP strain. The Fire Lab *C. elegans* Vector Kit was a gift from Andrew Fire (Addgene kit #
622 1000000001). Worm sorting was performed by Jérôme Belougne using the facilities of the
623 French National Functional Genomics platform, supported by the GIS IBiSA and Labex
624 INFORM. Some *C. elegans* strains were provided by the CGC, funded by NIH Office of Research
625 Infrastructure Programs (P40 OD010440). We thank Tim Schedl and the staff at WormBase for
626 amazing community work including the maintenance of a curated database, Meera Sundaram,
627 Jonathan Ewbank, Michel Labouesse and Helge Großhans for discussions and comments on
628 the manuscript. We thank the imaging core facility (ImagImm) of the Centre d'Immunologie
629 de Marseille-Luminy (CIML) supported by the French National Research Agency through the
630 "Investments for the Future" program (France-BioImaging, ANR-10-INBS-0004).
631

Funding

The project leading to this publication has received funding from the French National Research Agency ANR-22-CE13-0037-01, ANR-10-INBS-0004-01 (France BioImaging) and France 2030, the French Government program managed by the French National Research Agency (ANR-16-CONV-0001) and from Excellence Initiative of Aix-Marseille University - A*MIDEX and institutional grants from CNRS, Aix Marseille University. Supported by the Biotechnology and Biological Sciences Research Council and the NSF Directorate for Biological Sciences (BB/X012492/1) to AA, the National Institutes of Health to ADC (NIH R35GM134970) and JDW (NIH R21OD033663).

References

Abramson, J., Adler, J., Dunger, J., Evans, R., Green, T., Pritzel, A., Ronneberger, O., Willmore, L., Ballard, A. J., Bambrick, J., et al. (2024). Accurate structure prediction of biomolecular interactions with AlphaFold 3. *Nature* 630, 493–500.

Adams, J. R. G., Pooranachithra, M., Jyo, E. M., Zheng, S. L., Goncharov, A., Crew, J. R., Kramer, J. M., Jin, Y., Ernst, A. M. and Chisholm, A. D. (2023). Nanoscale patterning of collagens in *C. elegans* apical extracellular matrix. *Nat Commun* 14, 7506.

Aggad, D., Brouilly, N., Omi, S., Essmann, C. L., Dehapiot, B., Savage-Dunn, C., Richard, F., Cazevieille, C., Politi, K. A., Hall, D. H., et al. (2023). Meisosomes, folded membrane microdomains between the apical extracellular matrix and epidermis. *Elife* 12, e75906.

Aljohani, M. D., El Mouridi, S., Priyadarshini, M., Vargas-Velazquez, A. M. and Frøkjær-Jensen, C. (2020). Engineering rules that minimize germline silencing of transgenes in simple extrachromosomal arrays in *C. elegans*. *Nat Commun* 11, 6300.

Altschul, S. F., Gish, W., Miller, W., Myers, E. W. and Lipman, D. J. (1990). Basic local alignment search tool. *J Mol Biol* 215, 403–410.

Ashkenazy, H., Abadi, S., Martz, E., Chay, O., Mayrose, I., Pupko, T. and Ben-Tal, N. (2016). ConSurf 2016: an improved methodology to estimate and visualize evolutionary conservation in macromolecules. *Nucleic Acids Research* 44, W344.

Balasubramaniam, B., Topalidou, I., Kelley, M., Meadows, S. M., Funk, O., Ailion, M. and Fay, D. S. (2023). Effectors of anterior morphogenesis in *C. elegans* embryos. *Biol Open* 12, bio059982.

Birnbaum, S. K., Cohen, J. D., Belfi, A., Murray, J. I., Adams, J. R. G., Chisholm, A. D. and Sundaram, M. V. (2023). The proprotein convertase BLI-4 promotes collagen secretion prior to assembly of the *Caenorhabditis elegans* cuticle. *PLoS Genet* 19, e1010944.

Buchan, D. W. A. and Jones, D. T. (2019). The PSIPRED Protein Analysis Workbench: 20 years on. *Nucleic Acids Research* 47, W402.

Chiyoda, H., Kume, M., Del Castillo, C. C., Kontani, K., Spang, A., Katada, T. and Fukuyama, M. (2021). *Caenorhabditis elegans* PTR/PTCHD PTR-18 promotes the clearance of extracellular hedgehog-related protein via endocytosis. *PLoS Genet* 17, e1009457.

Cohen, J. D. and Sundaram, M. V. (2020). *C. elegans* Apical Extracellular Matrices Shape Epithelia. *J Dev Biol* 8, E23.

Cohen, J. D., Bermudez, J. G., Good, M. C. and Sundaram, M. V. (2020). A *C. elegans* Zona Pellucida domain protein functions via its ZPc domain. *PLoS Genet* 16, e1009188.

677 Cottee, M. A., Muschalik, N., Wong, Y. L., Johnson, C. M., Johnson, S., Andreeva, A., Oegema,
678 K., Lea, S. M., Raff, J. W. and van Breugel, M. (2013). Crystal structures of the
679 CPAP/STIL complex reveal its role in centriole assembly and human microcephaly.
680 *eLife* 2, e01071.
681 Couillault, C., Pujol, N., Reboul, J., Sabatier, L., Guichou, J. F., Kohara, Y. and Ewbank, J. J.
682 (2004). TLR-independent control of innate immunity in *C. elegans* by the TIR domain
683 adaptor protein TIR-1, an ortholog of human SARM. *Nat Immunol* 5, 488–494.
684 Cox, G. N., Laufer, J. S., Kusch, M. and Edgar, R. S. (1980). Genetic and Phenotypic
685 Characterization of Roller Mutants of *Caenorhabditis elegans*. *Genetics* 95, 317–339.
686 Cox, G. N., Kusch, M. and Edgar, R. S. (1981). Cuticle of *Caenorhabditis elegans*: its isolation
687 and partial characterization. *J Cell Biol* 90, 7–17.
688 Craig, D. B. and Dombkowski, A. A. (2013). Disulfide by Design 2.0: a web-based tool for
689 disulfide engineering in proteins. *BMC Bioinformatics* 14, 346.
690 Davis, M. W. and Jorgensen, E. M. (2022). ApE, A Plasmid Editor: A Freely Available DNA
691 Manipulation and Visualization Program. *Front Bioinform* 2, 818619.
692 Davis, P., Zarowiecki, M., Arnaboldi, V., Becerra, A., Cain, S., Chan, J., Chen, W. J., Cho, J., da
693 Veiga Beltrame, E., Diamantakis, S., et al. (2022). WormBase in 2022-data, processes,
694 and tools for analyzing *Caenorhabditis elegans*. *Genetics* 220, iyac003.
695 Dickinson, D. J., Pani, A. M., Heppert, J. K., Higgins, C. D. and Goldstein, B. (2015).
696 Streamlined Genome Engineering with a Self-Excising Drug Selection Cassette.
697 *Genetics* 200, 1035–1049.
698 Dierking, K., Polanowska, J., Omi, S., Engelmann, I., Gut, M., Lembo, F., Ewbank, J. J. and
699 Pujol, N. (2011). Unusual regulation of a STAT protein by an SLC6 family transporter
700 in *C. elegans* epidermal innate immunity. *Cell Host Microbe* 9, 425–35.
701 Dodd, W., Tang, L., Lone, J. C., Wimberly, K., Wu, C. W., Consalvo, C., Wright, J. E., Pujol, N.
702 and Choe, K. P. (2018). A Damage Sensor Associated with the Cuticle Coordinates
703 Three Core Environmental Stress Responses in *C. elegans*. *Genetics* 208, 1467–1482.
704 Doitsidou, M., Poole, R. J., Sarin, S., Bigelow, H. and Hobert, O. (2010). *C. elegans* Mutant
705 Identification with a One-Step Whole-Genome-Sequencing and SNP Mapping
706 Strategy. *PLoS ONE* 5, e15435.
707 Drozdetskiy, A., Cole, C., Procter, J. and Barton, G. J. (2015). JPred4: a protein secondary
708 structure prediction server. *Nucleic Acids Research* 43, W389.
709 El Mouridi, S., Peng, Y. and Frøkjær-Jensen, C. (2020). Characterizing a strong pan-muscular
710 promoter (Pmlc-1) as a fluorescent co-injection marker to select for single-copy
711 insertions. *microPublication Biology* 2020, 10.17912/micropub.biology.000302.
712 El Mouridi, S., AlHarbi, S. and Frøkjær-Jensen, C. (2021). A histamine-gated channel is an
713 efficient negative selection marker for *C. elegans* transgenesis. *microPublication*
714 *Biology* 2021, 10.17912/micropub.biology.000349.
715 Fire, A., Harrison, S. W. and Dixon, D. (1990). A modular set of lacZ fusion vectors for
716 studying gene expression in *Caenorhabditis elegans*. *Gene* 93, 189–198.
717 Forman-Rubinsky, R., Cohen, J. D. and Sundaram, M. V. (2017). Lipocalins Are Required for
718 Apical Extracellular Matrix Organization and Remodeling in *Caenorhabditis elegans*.
719 *Genetics* 207, 625–642.
720 Gerstein, M. B., Lu, Z. J., Van Nostrand, E. L., Cheng, C., Arshinoff, B. I., Liu, T., Yip, K. Y.,
721 Robilotto, R., Rechtsteiner, A., Ikegami, K., et al. (2010). Integrative analysis of the
722 *Caenorhabditis elegans* genome by the modENCODE project. *Science* 330, 1775–
723 1787.

Ghaddar, A., Armingol, E., Huynh, C., Gevirtzman, L., Lewis, N. E., Waterston, R. and O'Rourke, E. J. (2023). Whole-body gene expression atlas of an adult metazoan. *Science Advances* 9, eadg0506.

Haase, R., Royer, L. A., Steinbach, P., Schmidt, D., Dibrov, A., Schmidt, U., Weigert, M., Maghelli, N., Tomancak, P., Jug, F., et al. (2020). CLIJ: GPU-accelerated image processing for everyone. *Nat Methods* 17, 5–6.

Hendriks, G.-J., Gaidatzis, D., Aeschimann, F. and Großhans, H. (2014). Extensive oscillatory gene expression during *C. elegans* larval development. *Mol Cell* 53, 380–392.

Johnson, L. C., Vo, A. A., Clancy, J. C., Myles, K. M., Pooranachithra, M., Aguilera, J., Levenson, M. T., Wohlenberg, C., Rechtsteiner, A., Ragle, J. M., et al. (2023). NHR-23 activity is necessary for *C. elegans* developmental progression and apical extracellular matrix structure and function. *Development* 150, dev201085.

Jumper, J., Evans, R., Pritzel, A., Green, T., Figurnov, M., Ronneberger, O., Tunyasuvunakool, K., Bates, R., Žídek, A., Potapenko, A., et al. (2021). Highly accurate protein structure prediction with AlphaFold. *Nature* 596, 583–589.

Kamath, R. S., Fraser, A. G., Dong, Y., Poulin, G., Durbin, R., Gotta, M., Kanapin, A., Le Bot, N., Moreno, S., Sohrmann, M., et al. (2003). Systematic functional analysis of the *Caenorhabditis elegans* genome using RNAi. *Nature* 421, 231–237.

Katsanos, D., Ferrando-Marco, M., Razzaq, I., Aughey, G., Southall, T. D. and Barkoulas, M. (2021). Gene expression profiling of epidermal cell types in *C. elegans* using Targeted DamID. *Development* 148, dev199452.

Katz, S. S., Barker, T. J., Maul-Newby, H. M., Sparacio, A. P., Nguyen, K. C. Q., Maybrun, C. L., Belfi, A., Cohen, J. D., Hall, D. H., Sundaram, M. V., et al. (2022). A transient apical extracellular matrix relays cytoskeletal patterns to shape permanent acellular ridges on the surface of adult *C. elegans*. *PLoS Genet* 18, e1010348.

Kim, D. hyun, Grün, D. and van Oudenaarden, A. (2013). Dampening of expression oscillations by synchronous regulation of a microRNA and its target. *Nat Genet* 45, 1337–1344.

Kussie, P. H., Gorina, S., Marechal, V., Elenbaas, B., Moreau, J., Levine, A. J. and Pavletich, N. P. (1996). Structure of the MDM2 Oncoprotein Bound to the p53 Tumor Suppressor Transactivation Domain. *Science* 274, 948–953.

Labed, S. A., Omi, S., Gut, M., Ewbank, J. J. and Pujol, N. (2012). The pseudokinase NIPI-4 is a novel regulator of antimicrobial peptide gene expression. *PLoS One* 7, e33887.

Lažetić, V. and Fay, D. S. (2017). Molting in *C. elegans*. *Worm* 6, e1330246.

Lee, S. H., Omi, S., Thakur, N., Taffoni, C., Belougne, J., Engelmann, I., Ewbank, J. J. and Pujol, N. (2018). Modulatory upregulation of an insulin peptide gene by different pathogens in *C. elegans*. *Virulence* 9, 648–658.

Macias, M. J., Wiesner, S. and Sudol, M. (2002). WW and SH3 domains, two different scaffolds to recognize proline-rich ligands. *FEBS Letters* 513, 30–37.

Martineau, C. N., Kirienko, N. V. and Pujol, N. (2021). Innate immunity in *C. elegans*. *Curr Top Dev Biol* 144, 309–351.

McMahon, L., Muriel, J. M., Roberts, B., Quinn, M. and Johnstone, I. L. (2003). Two sets of interacting collagens form functionally distinct substructures within a *Caenorhabditis elegans* extracellular matrix. *Mol Biol Cell* 14, 1366–1378.

Meeuse, M. W., Hauser, Y. P., Morales Moya, L. J., Hendriks, G.-J., Eglinger, J., Bogaarts, G., Tsiairis, C. and Großhans, H. (2020). Developmental function and state transitions of a gene expression oscillator in *Caenorhabditis elegans*. *Mol Syst Biol* 16, e9498.

771 Meeuse, M. W. M., Hauser, Y. P., Nahar, S., Smith, A. A. T., Braun, K., Azzi, C., Rempfler, M.
772 and Großhans, H. (2023). *C. elegans* molting requires rhythmic accumulation of the
773 Grainyhead/LSF transcription factor GRH-1. *EMBO J* 42, e111895.
774 Miao, R., Li, M., Zhang, Q., Yang, C. and Wang, X. (2020). An ECM-to-Nucleus Signaling
775 Pathway Activates Lysosomes for *C. elegans* Larval Development. *Dev Cell* 52, 21-
776 37.e5.
777 Minevich, G., Park, D. S., Blankenberg, D., Poole, R. J. and Hobert, O. (2012). CloudMap: A
778 Cloud-Based Pipeline for Analysis of Mutant Genome Sequences. *Genetics* 192, 1249.
779 Mistry, J., Chuguransky, S., Williams, L., Qureshi, M., Salazar, G. A., Sonnhammer, E. L. L.,
780 Tosatto, S. C. E., Paladin, L., Raj, S., Richardson, L. J., et al. (2021). Pfam: The protein
781 families database in 2021. *Nucleic Acids Res* 49, D412–D419.
782 Mok, D. Z. L., Sternberg, P. W. and Inoue, T. (2015). Morphologically defined sub-stages of *C.*
783 *elegans* vulval development in the fourth larval stage. *BMC Dev Biol* 15, 26.
784 Motohashi, K. (2015). A simple and efficient seamless DNA cloning method using SLiCE from
785 *Escherichia coli* laboratory strains and its application to SLiP site-directed
786 mutagenesis. *BMC Biotechnol* 15, 1–9.
787 Paysan-Lafosse, T., Blum, M., Chuguransky, S., Grego, T., Pinto, B. L., Salazar, G. A., Bileschi,
788 M. L., Bork, P., Bridge, A., Colwell, L., et al. (2023). InterPro in 2022. *Nucleic Acids*
789 *Research* 51, D418–D427.
790 Potter, S. C., Luciani, A., Eddy, S. R., Park, Y., Lopez, R. and Finn, R. D. (2018). HMMER web
791 server: 2018 update. *Nucleic Acids Research* 46, W200–W204.
792 Pujol, N., Cypowyj, S., Ziegler, K., Millet, A., Astrain, A., Goncharov, A., Jin, Y., Chisholm, A. D.
793 and Ewbank, J. J. (2008a). Distinct innate immune responses to infection and
794 wounding in the *C. elegans* epidermis. *Curr Biol* 18, 481–9.
795 Pujol, N., Zugasti, O., Wong, D., Couillault, C., Kurz, C. L., Schulenburg, H. and Ewbank, J. J.
796 (2008b). Anti-fungal innate immunity in *C. elegans* is enhanced by evolutionary
797 diversification of antimicrobial peptides. *PLoS Pathog* 4, e1000105.
798 Schwartz, M. L. and Jorgensen, E. M. (2016). SapTrap, a Toolkit for High-Throughput
799 CRISPR/Cas9 Gene Modification in Caenorhabditis elegans. *Genetics* 202, 1277–1288.
800 Serra, N. D., Darwin, C. B. and Sundaram, M. V. (2024). *Caenorhabditis elegans* Hedgehog-
801 related proteins are tissue- and substructure-specific components of the cuticle and
802 precuticle. *GENETICS* 227, iyae081.
803 Stiernagle, T. (2006). Maintenance of *C. elegans*. *Wormbook* 1.
804 Sun, S., Theska, T., Witte, H., Ragsdale, E. J. and Sommer, R. J. (2022). The oscillating Mucin-
805 type protein DPY-6 has a conserved role in nematode mouth and cuticle formation.
806 *Genetics* 220, iyab233.
807 Sundaram, M. V. and Pujol, N. (2024). The *Caenorhabditis elegans* cuticle and precuticle: a
808 model for studying dynamic apical extracellular matrices in vivo. *GENETICS* 227,
809 iyae072.
810 Taffoni, C., Omi, S., Huber, C., Mailfert, S., Fallet, M., Rupprecht, J.-F., Ewbank, J. J. and Pujol,
811 N. (2020). Microtubule plus-end dynamics link wound repair to the innate immune
812 response. *Elife* 9, e45047.
813 Thein, M. C., McCormack, G., Winter, A. D., Johnstone, I. L., Shoemaker, C. B. and Page, A. P.
814 (2003). *Caenorhabditis elegans* exoskeleton collagen COL-19: An adult-specific
815 marker for collagen modification and assembly, and the analysis of organismal
816 morphology. *Developmental Dynamics* 226, 523–539.

817 Thomas, P. D., Ebert, D., Muruganujan, A., Mushayahama, T., Albou, L.-P. and Mi, H. (2022).
818 PANTHER: Making genome-scale phylogenetics accessible to all. *Protein Sci* 31, 8–22.
819 Tsiairis, C. and Großhans, H. (2021). Gene expression oscillations in *C. elegans* underlie a new
820 developmental clock. *Curr Top Dev Biol* 144, 19–43.
821 Vuong-Brender, T. T. K., Suman, S. K. and Labouesse, M. (2017). The apical ECM preserves
822 embryonic integrity and distributes mechanical stress during morphogenesis.
823 *Development* 144, 4336–4349.
824 Zhang, X., Harding, B. W., Aggad, D., Courtine, D., Chen, J. X., Pujol, N. and Ewbank, J. J.
825 (2021). Antagonistic fungal enterotoxins intersect at multiple levels with host innate
826 immune defences. *PLoS Genet* 17, e1009600.
827 Ziegler, K., Kurz, C. L., Cypowyj, S., Couillault, C., Pophillat, M., Pujol, N. and Ewbank, J. J.
828 (2009). Antifungal innate immunity in *C. elegans*: PKCdelta links G protein signaling
829 and a conserved p38 MAPK cascade. *Cell Host Microbe* 5, 341–52.
830 Zugasti, O., Bose, N., Squiban, B., Belougne, J., Kurz, C. L., Schroeder, F. C., Pujol, N. and
831 Ewbank, J. J. (2014). Activation of a G protein-coupled receptor by its endogenous
832 ligand triggers the innate immune response of *C. elegans*. *Nat Immunol* 15, 833–8.
833 Zugasti, O., Thakur, N., Belougne, J., Squiban, B., Kurz, C. L., Soulé, J., Omi, S., Tichit, L., Pujol,
834 N. and Ewbank, J. J. (2016). A quantitative genome-wide RNAi screen in *C. elegans* for
835 antifungal innate immunity genes. *BMC Biol* 14, 35.
836
837

Supplementary Materials

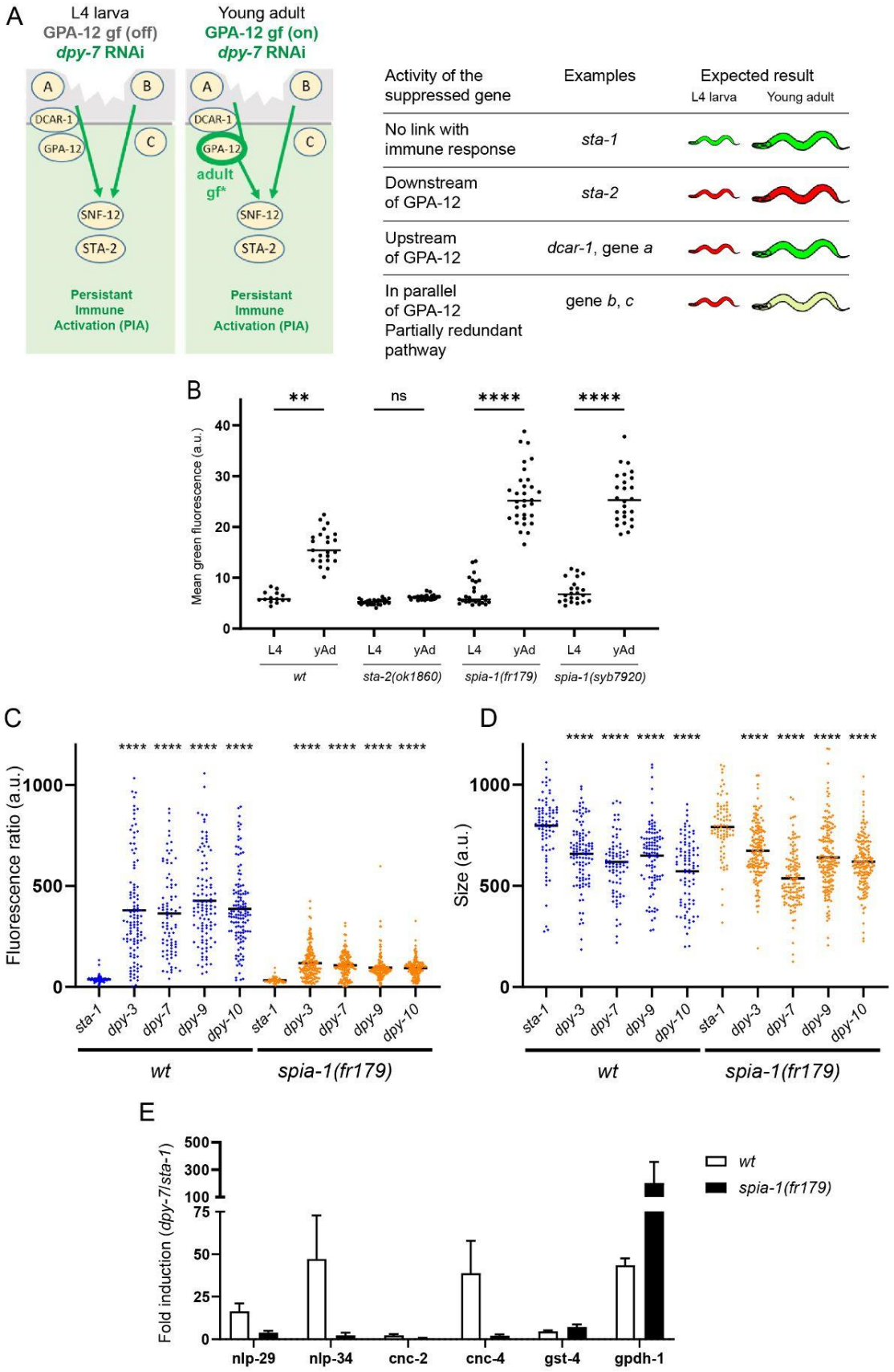

840 **Fig S1**. (A) In the suppressor screen, we triggered a PIA in the strain IG1389 by inactivating *dpy-7* by
841 RNAi (left). In this strain, the state of the immune response is monitored (*frIs7* construct; green
842 fluorescence off=inactive, green fluorescence on=active) and GPA-12 is constitutively active in the
843 adult (*frIs30*). Different scenarios are expected depending on the gene affected after EMS-induced
844 mutagenesis (right). (B) Quantification of relative green fluorescence in worms carrying *frIs7* and *frIs30*
845 constructs, but without *dpy-7* RNAi inactivation, in L4 and young adults (yAd); n>14. Only the
846 inactivation of a gene acting downstream of GPA-12 (e.g. *sta-2*) leads to the suppression of the green
847 fluorescence in adults. (C-D) Quantification with the Biosort of the ratio between *nlp-29*p::GFP
848 intensity and size (C) and of the size of the worms (D) in *wt* or *spia-1(fr179)* adults following RNAi
849 inactivation of the 4 furrow collagen genes and the *sta-1* control; n>70, one of 3 independent
850 experiments. *spia-1(fr179)* does not suppress the short size induced via inactivation of the 4 furrow
851 collagen genes. Statistical comparisons were made by comparing to the corresponding *sta-1* control.
852 $**p < 0.01$; $****p < 0.0001$. (E) mRNA levels of *nlp-29*, *nlp-34*, *cnc-2*, *cnc-4*, *gst-4* and *gpdh-1* were
853 quantified by qPCR in wild-type and *spia-1(fr179)* worms upon RNAi inactivation of *sta-1* or *dpy-7*, in
854 three independent experiments. The mean fold-changes between the *dpy-7* and *sta-1* levels are
855 represented. In *spia-1(fr179)*, the transcription of AMPs genes including *nlp-29, nlp-34* and *cnc-4* were
856 reduced, contrary to the transcription of *gst-4* and *gpdh-1*, the latter being increased.
857
858

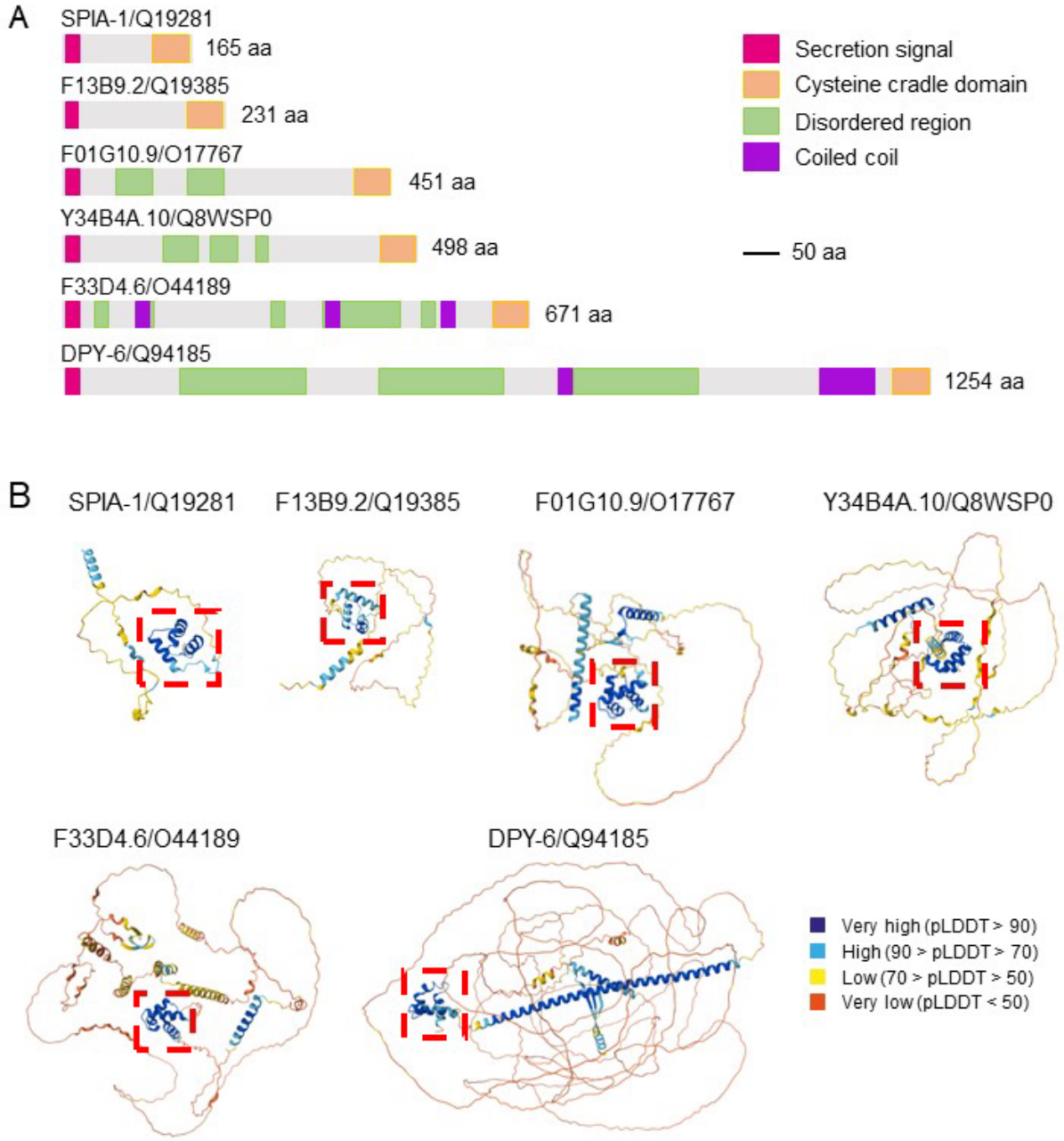

Fig S2. (A) Domain organisation of the 6 CCD-aECM proteins in *C. elegans*, as annotated in InterPro (Mistry et al., 2021; Paysan-Lafosse et al., 2023) and (B) structural models predicted with AlphaFold (Abramson et al., 2024; Jumper et al., 2021), rendered with the Predicted Local Distance Difference Test score (pLDDT), which indicates how well a predicted protein structure matches protein data bank structure information and multiple sequence alignment data.

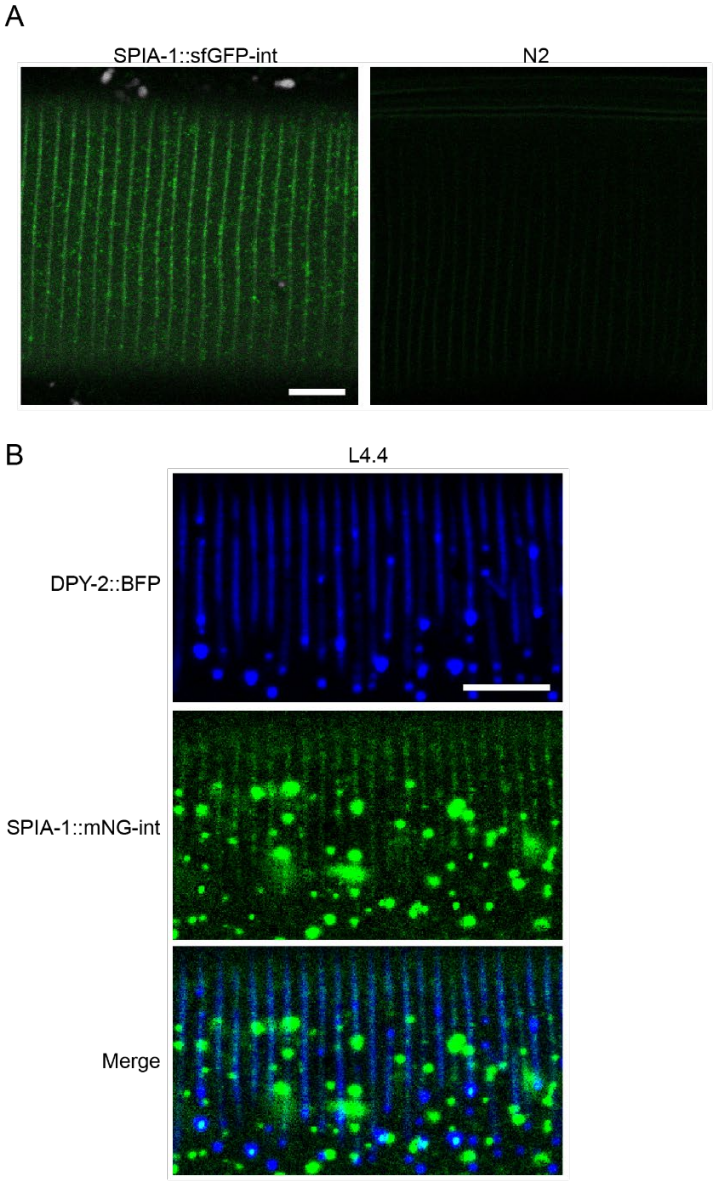

Fig S3. (A) The confocal image of the SPIA-1::sfGFP reporter (GFP-int) in the adult shown in figure 4D is presented aside from an adult N2 imaged using same illumination conditions; n>5, scale bar, 5 µm. (B) Zoom on the furrows in the L4.4 shown in Fig 4F. Both single channels and the merge are shown, as depicted. NUC-1::mCherry is not shown for clarity; scale bar, 5 µm.

873

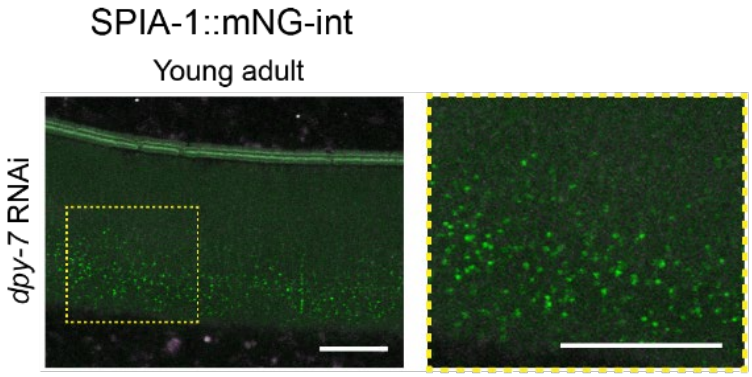

874

875 **Fig S4**. Representative images of SPIA-1::mNG-int young adults following *dpy-7* inactivation. To
876 compare with Fig 5D. A ~2.5 times magnification of the area contained in the dashed rectangle is
877 provided on the far right; n>5, scale bar, 10 µm.

878

879
880

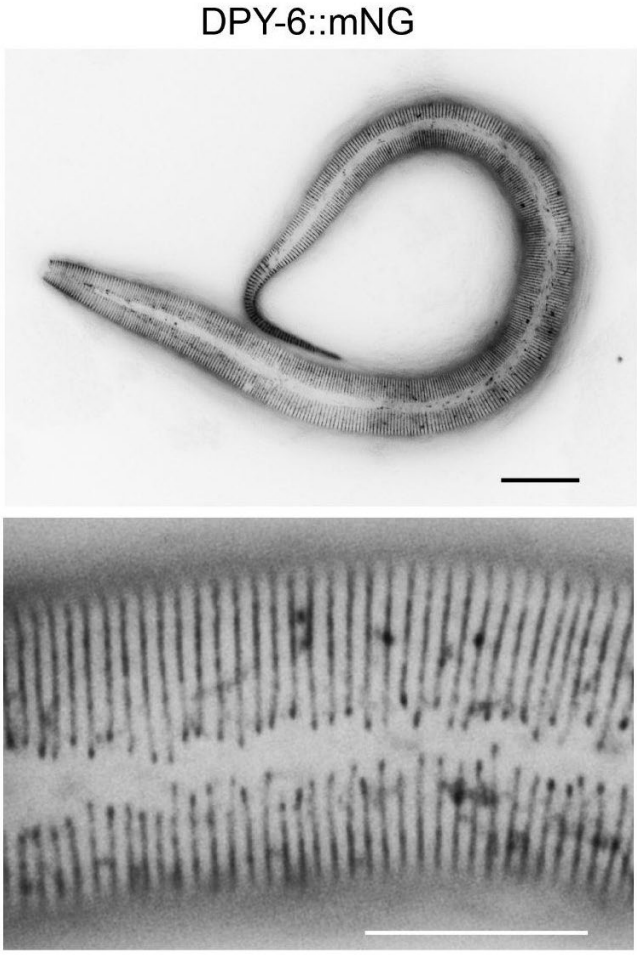

881
882
883 **Fig S5**. Representative fluorescent images of the furrow localisation of DPY-6::mNG-int, in a L1 (top) or
884 L2 larva (bottom); n>5, scale bar, 20 µm (top), 10 µm (bottom).
885
886

887 **Supplementary movie**

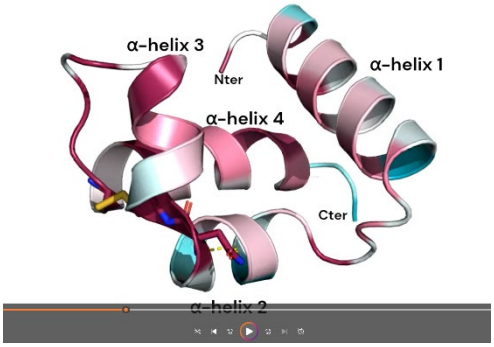

888

889 AlphaFold2 prediction of the SPIA-1 conserved CCD-aECM rendered in surface and cartoon. The model
890 is coloured according to Consurf conservation scores across SPIA-1 orthologues in nematodes. The
891 movie features the invariant cysteine residues predicted to form disulfide bonds (Cys138 with Cys150,
892 Cys115 with Cys160), residues involved in hydrogen bonds probably stabilising the CCD-aECM (Trp133
893 with Asn137, Asp129 with Ala132, Leu110 with Ser159), aromatic residues lining the groove and
894 defining a highly hydrophobic interface (Tyr121, Tyr125, Trp133, Phe140, Tyr144), and other conserved
895 residues with predicted structural and functional roles (Gly126, Asp129, Pro146). Numbers indicate
896 the position of the amino acid in the *C. elegans* SPIA-1 protein sequence.

897 https://filesender.renater.fr/?s=download&token=5d52b645-c659-48da-abd3-291e7aae08dc

898

899